Scatterometry Using Speckle Correlations

Submitted in partial fulfillment of the requirements for the degree of

Doctor of Philosophy

in

Electrical and Computer Engineering

Bakari Hassan

B.S., Applied Physics, Morehouse College

B.S., Aerospace Engineering, University of Michigan

M.S., Electrical Engineering and Computer Science, University of California Los Angeles

Carnegie Mellon University

Pittsburgh, Pennsylvania

December 2024

Abstract

Material acquisition describes the process of inferring properties of materials from observations. We are interested in acquiring a scattering property of materials called the scattering phase function which governs the spherical directionality of scattered light intensity. The phase function largely influences the translucent appearance of materials and is driven by material properties such as the type and size of particles in the medium, so it is essential for characterization.

One approach relies on reducing sample optical density such that light paths through the material are scattered once on average. The phase function is then inferred from the relative scattered intensities in different directions. However, this method is limited to classes of materials that can be sliced thinly or diluted. An alternative approach estimates the scattering phase function by inverting the radiative transfer equation. Although it does not require isolating single-scattering events, it is costly and relies on good initialization due to it use of stochastic gradient descent. Efficient, closed-form approaches that rely on the memory effect have been developed for material acquisition from thick samples. By illuminating a sample with coherent laser light and capturing speckle patterns, correlations within the memory effect range allow the single-scattered component to be measured in the presence of high-order scattering. However, the proposed acquisition system measures the scattering phase function over a small angular range of a few degrees due to inherent angular limits of a 4f system.

In this work, we detail material acquisition over angular ranges approaching 180° via scatterometry. Our approach is similar to reflectometry wherein we use two sources fixed to a goniometer that rotates around a sample. We use two mutually coherent laser beams separated by a small angle to maximize speckle correlation. Their respective speckle patterns are acquired using a camera, and the phase function in the mean direction of the two laser beams is proportional to the speckle correlation. The goniometer then rotates the illuminators about the sample to measure the scattering phase function over a large range without the angular limitations inherent in 4f imaging systems. Our results are relevant to graphics applications such as photorealistic augmented reality as well as areas outside graphics and vision such as non-invasive medical diagnostics, remote sensing, and particle sizing for quality assurance.

Contents

List of Figures

List of Tables

Chapter 1

Introduction

Scattering materials are ubiquitous, and they play key roles in fields such as tissue and blood analysis in medical imaging used to classify tumors as malignant or benign, produce characterization in the agriculture industry, soil analysis and material identification in remote sensing, and particle size estimates for quality assurance and shelf life estimates of cosmetics. These applications have widespread societal impacts, and they benefit from a deeper understanding of the optical properties of scattering. However, the complex nature scattering poses challenges for advancements in end applications. As a result, there has been a variety of approaches to understanding the underlying scattering phenomena. One class of approaches focuses on optically thick materials whose analysis can be approximated using the diffusion approximation. Monte-Carlo rendering has been used to consider materials of arbitrary thickness. However, they are computationally expensive and require proper initialization. The final class works under the single-scattering approximation and focuses on materials where single-scattering can be isolated. One way to isolate single-scattering is to dilute materials so light scatters once on average. This allows simple characterization methods similar to reflectometry for a narrow class of materials. Single-scattering can also be isolated for multi-scattering materials by using coherent illumination to compute scattering statistics dominated by single-scattered light. However, these methods have been limited to small scattering angles. The goal of this thesis is to combine the advantages of both approaches under the single-scattering approximation. We compute correlations to isolate single-scattered light in multi-scattering materials, and we expand the range of scattering angles from 8° to greater than 100° using scatteometry to make direct and accurate measurements for a broad class of materials.

1.0.1 Thesis contributions

In this thesis, we introduce a novel scatterometry system for material acquisition over a broad range of scattering angles exceeding 100°. We are particularly interested in opaque materials that exhibit multi-scattering. This thesis establishes the design approach for scatterometry under the single-scattering approximation as well as the calibration and alignment processes. The high-level design and unique aspects are detailed in Section _, the calibration and alignment processes are covered in Sections _, and results are discussed in Section _.

1.1 Material acquisition (related work)

Material acquisition is the task of recovering the intrinsic properties of materials based on their appearance. It is of great importance in many applications. For example, tumors can be detected and classified as malignant or non-malignant [5]; important blood properties such as red and white blood counts can also be analyzed [4, 10]; in materials science, material acquisition is used to validate the fidelity and shelf life of material samples [33]; and the chemical compositions of nanodispersions can be inferred for particle sizing applications [30]. Material acquisition methods can be grouped into three categories depending on the ratio of the mean free path (expected distance traveled by a photon in the medium) to the characteristic size of the scattering volume. We summarize these categories in turn, as well as several common phase function models.

Inverse radiative transport [2] is studied heavily in graphics as well as the physical and biomedical sciences. While inverse radiative transport methods for scattering media fall into three main categories, methods using the *diffusion* approximation focus on optically thick media where high-order scattering is dominant. While this approximation simplifies inference and is suitable for both homogeneous and heterogeneous materials [12, 24, 29], it introduces parameter ambiguities. Similarity relations are hierarchical parameter relationships that allow scattering parameters to be altered without significantly altering the medium's spatial properties. These relations can be derived from transport equations to accelerate Monte Carlo simulations [36]. However, a radiance field computed via Monte Carlo simulations can be described by multiple, distinct sets of parameters, and finding mulutiple candidate solution sets is generally challenging. Parameter space warping and exploiting similarity relations have improved the efficiency of iterative solvers [37].

Rather than focusing purely on high-order scattering, another class of methods considers all paths of arbitrary lengths. Given a set of input images, they estimate material parameters whose combinations closely match the inputs when simulated using Monte-Carlo rendering [11, 28]. Differentiable rendering determines the effects of changes in scattering parameters by estimating derivatives of images. Traditionally, these estimtes have been approximate models that ignore complex light transport effects such as subsurface scattering and inter-reflections [22]. Differentiable Monte Carlo rendering overcomes these limiations by computing derivatives while accounting for all light transport effects [15, 17, 21, 26, 27]. Machine learning approaches offer lower computational complexity at the cost of reduced robustness and diminished physically accurate solutions. Encoder networks can be paired with Monte Carlo renderers to improve their generalization to scenes with unseen geometry and light sources [35, 8]. Energy losses in neural radiance fields are mitigated by efficient indirect illumination estimation via spherical harmonics [38]. While these approach are more general in nature and can handle arbitrarily thick materials, they are computationally expensive and require proper initialization.

The final class of methods are based on the *single scattering* approximation. The first approach assumes the medium is thin enough optically such that photons only scatter once when traveling through the medium. Since the scattering phase function is defined in terms of single-scattering, this allows the phase function to be observed directly. Although this method is as simple, it is limited to a narrow classes of materials such as gases and liquids of low viscosity [25]. Viscous liquids and thin solids can be acquired by illuminating materials with coherent light and computing the correlations of speckle images. Speckle image correlations are dominated by single-scattered light, and [1] showed that the phase function is proportional to the square root of the correlation and can be computed using a closed-form equation. However, this method is limited to measuring phase functions up to 8° due to aberrations.

The Henyey-Greenstein model is used widely due to its relative flexibility considering it is a single-parameter model [19]. It is controlled by an anisotropy parameter $g \in [-1, 1]$ that can be used to model backward and forward scattering. However, its simplicity limits its ability to accurately model other scattering regimes such as Rayleigh scattering that occurs when scattering particles are small compared to the wavelength [9, 31]. Alternatives to this model include using linear combinations of two Henyey-Greenstein lobes (forward and backward) as well as a two-parameter model for highly anisotropic scattering present in human blood [32]. However, there remain common materials that are not well-represented by these models such as soaps and waxes [16]. Hara et al. modify the HG phase function by adding side-lobes resembling the von Mises-Fisher distribution which closely resembles scattering of materials such as soaps and waxes that exhibit forward scattering with significant side scattering [13, 18].

1.2 Background

Scattering refers to the behavior of light when it interacts with a medium containing particles or when light interacts with the interface between two mediums of different properties. When light interacts with a particle in a scattering medium, the scattering event generates many additional light paths that all undergo additional scattering events before arriving at the observer. Scattering is essential to the appearance of food, liquids, skin, and other translucent materials, and an understanding of scattering is critical to determining their appearances. Under incoherent illumination, scattering produces smooth highlights with gradual falloff from the area of illumination. However, under coherent illumination, scattering produces speckle. Although speckle may appear random, it has a strong structure determined by the properties of the illumination and the scattering medium.

- Here's why we can reduce that to SS
- Once we have SS, this is how we make measurements

1.2.1 Scattering material representation

Scattering materials are generally composed of small particles with varying refractive properties we describe through the bulk statistical properties of the material. We use three statistical properties to parameterize the scattering material. The extinction coefficient describes the extinction cross-section of the scattering particles per unit volume. It is therefore proportional to the density of scattering particles inside the material. The extinction coefficient is the sum of the absorption and scattering coefficients $\sigma_t = \sigma_a + \sigma_s$ which represent, respectively, the portion of light absorbed and scattered per unit length along the path. The material's phase function $\rho(\arccos(\hat{\mathbf{i}} \cdot \hat{\mathbf{v}}))$ describes the directionality of scattered light and determines the portion of light scattered towards direction $\hat{\mathbf{v}}$ when a scatterer is illuminated from direction $\hat{\mathbf{i}}$. A scatterer's phase function is dictated by its shape and refractive index. Phase functions for spherical particles can be computed analytically using Mie theory[6, 14, 20]. ρ is generally assumed to be isotropic. This means its value depends only on the inner product of the illumination and viewing directions, and not on the absolute directions. This may be relaxed by adding an anisotropy parameter $-1 \leq g \leq 1$ where $g = -1$ corresponds to fully backward scattering, $g = 0$ means light is scattered equally in all directions, and $g = 1$ is full forward scattering. The mean free path (MFP) of a material is defined as the average distance light travels inside the volume between two successive scattering events. The MFP is the inverse of the extinction coefficient $MFP = 1/\sigma_t$. When working with scattering volumes, it is common to express its geometric dimensions with respect to the MFP. For example, a volume with optical depth $OD = 4$ means its thickness is $4 \cdot MFP$. This means that light traveling through the medium is scattered four times in average.

Our work is primarily interested in the phase function ρ and will not discuss scattering coefficients. Our work seeks to acquire ρ as a general function and does not assume common parameterizations such as the Henyey-Greenstein phase function [19].

$$p_{HG}(\theta) = \frac{1}{4\pi} \frac{1 - g^2}{(1 + g^2 - 2g \cos \theta)^{3/2}} \tag{1.1}$$

1.2.2 Phase function from speckle images

Validating extended range phase functions Phase functions can be validated by comparing correlations to results computed from full Monte-Carlo simulations. Monodispersions of microscopic silica beads are well-suited for validation because their scattering effects are well described by Mie theory. Alterman et al. validate their results by comparing closed-form correlations from Equation **??** to results to a Monte-Carlo simulator [3] that has been verified against an accurate wave solver [34]. We assess our results in two. First, we verify our acquisition setup and single-scattering computations by comparing acquired $3\mu m$ and $10\mu m$ monodispersions to Mie theory. We then validate results for non-monodisperse samples that are not easily characterized for simulation (e.g., mustard, milk, honey) by comparing our acquired phase functions to those acquired by Alterman et al. over angular ranges up to approximately 8 degrees [1]. Given extended-range verification against theory and limited-range validation with related work, we consider our extended-range measurements valid.

Phase function from single scattering models A simple method for measuring phase functions is acquiring optically thin samples that scatter light once on average ($OD \approx 1$). This method is as simple as reflectometry: we illuminate a sample in direction $\boldsymbol{i}$ and measure the light received in direction $\boldsymbol{v}$, and the phase function is the portion of energy corresponding to scattering angle $\arccos(\hat{\mathbf{i}} \cdot \hat{\mathbf{v}})$. In the paraxial regime, we can apply the small-angle approximation to equate the scattering angle as the norm of the displacement vector between the illuminating and viewing directions $\boldsymbol{\tau} = \hat{\mathbf{v}} - \hat{\mathbf{i}}$, and $|\boldsymbol{\tau}| = \arccos(\hat{\mathbf{i}} \cdot \hat{\mathbf{v}})$. This method fails with increasing material thickness due to multiple scattering.

1.3 Thesis contributions

Chapter 2

Speckle Correlation

Chapter 3

Scatterometer Design

In this chapter, we delve into the scatterometer design. We discuss the three main components of the scatterometer and their functions. We also detail unique design challenges for each component and any associated custom parts/accommodations that were necessary.

3.1 System design

Our scatterometer (detailed in Figures 3.1 and 3.2) consists of two mutually coherent, collimated beams of wavelength 532 nm separated vertically by a small angle of approximately 4° (assumed to be within the memory effect range for materials of interest). Both beams are attached to a stage that rotates the beams azimuthally about a scattering sample located on the stage's rotation axis. The intensity of scattered light is measured by a stationary camera as the beams are swept through a range of approximately 180°. The correlation of both beams' speckle images at a given azimuthal angle is proportional to the scattering phase function as a function of angle.

There are three primary components for acquisition. The first is the acquisition camera which we use to record speckle images. The second is the illuminator assembly which adjusts the angular illuminator separation and the azimuthal illumination direction relative to the acquisition camera. The third is the sample assembly which orients and positions the sample such that it is located on the azimuthal rotation axis of the illuminator assembly and maximal light is scattered towards the acquisition camera.

3.1.1 Acquisition camera

The acquisition camera must record high-contrast speckle images and assign directions to light arriving at the camera. A desirable camera and lens combination is one that maximizes angular resolution and

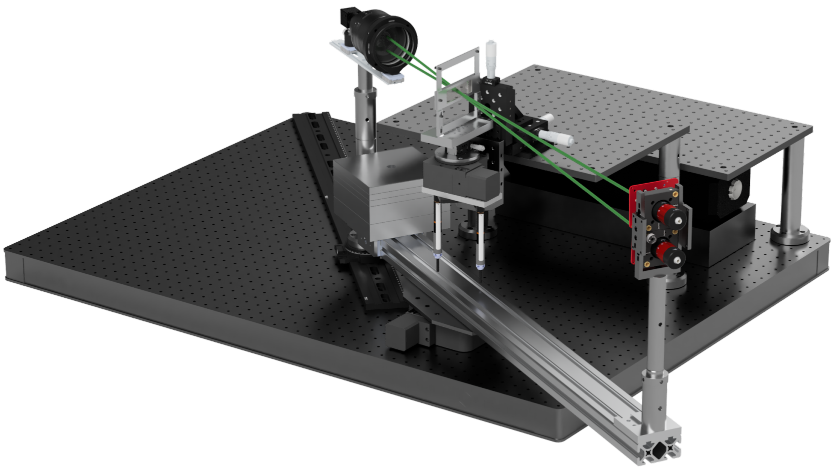

Figure 3.1: CAD rendering of speckle correlation scatterometer

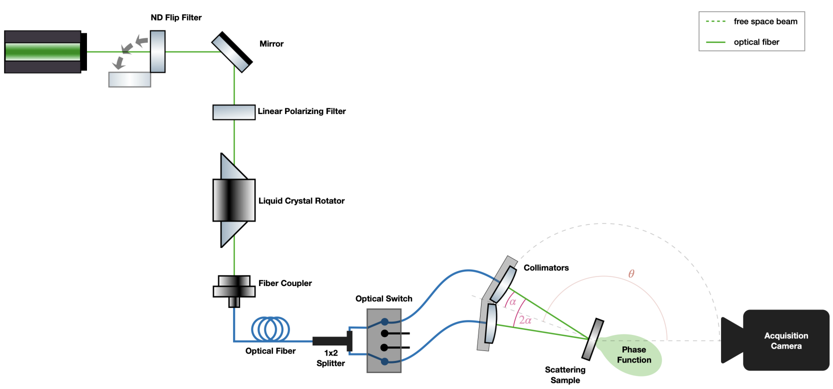

Figure 3.2: Light path diagram for speckle correlation scatterometer

light efficiency. Therefore, we choose a camera with a large sensor and small pixel pitch, and a fast lens focused at infinity with a long focal length.

Lens Focal Length Computing the speckle correlation from images produced by the two illuminators requires both beams to fall within the camera's FOV. Since we maximize single-scattered light by minimizing the illuminator separation, a lens with a small FOV corresponds to illuminators with a small angular separation. However, due to the finite size of the kinematic mounts, there is a minimum vertical separation. This minimum vertical separation and the FOV-limited angle between the beams define a triangle whose length is the distance from the illuminators' kinematic mounts to the scattering sample. An 85 mm lens allows a small beam angle 2.47° relative to horizontal and an overall setup size that complies with space constraints.

We use a FLIR Grasshopper scientific camera model GS3-PGE-91S6M-C with an AF-S Nikkor 85mm f/1.4G lens for acquisition.

Table 3.1: Acquisition camera specifications

Property	**Spec**
Camera Model	GS3-PGE-91S6M-C
Resolution	3376×2704
Megapixels	9.1
Pitch	3.69 μm
Sensor	Sony ICX814
Sensor Type	CCD
Sensor Size	12×10 mm
Spectrum	Mono
Lens Make	Nikkor
Lens Focal Length	85 mm
Lens Aperture	f/1.4
Lens Working Distance	∞

3.1.2 Illuminator assembly

The illuminator motion assembly controls the illumination beams' directions both in azimuth and elevation. The primary design considerations are high angular resolution and repeatability for fine control of the illumination configuration, and structural stability to minimize vibrations. Each illuminator is attached to a 2-axis kinematic mount that allows $\pm 5°$ in tip and $\pm 3°$ in tilt. Both kinematic mounts are attached to a custom collimator mount that minimizes their vertical separation while complying with the FOV constraint of $4.93°$ between the illuminators. The collimator mount is attached to the azimuthal rotation stage via an aluminum extrusion.

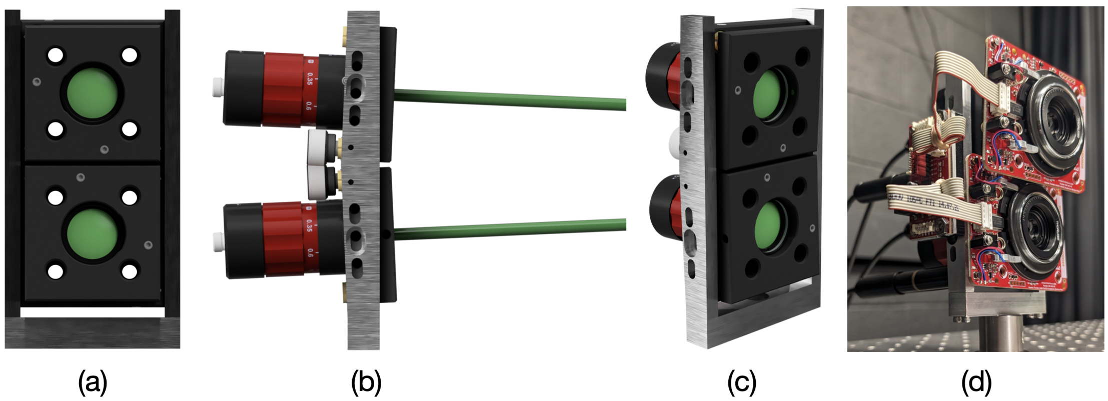

Figure 3.3: (a) CAD front view of collimator mount; (b) CAD side view showing the relative orientations of illumination beams; (c) CAD perspective view; (d) Fully assembled collimator mount which controls vertical and angular illuminator separation. Beam diameter is also controlled using motorized iris diaphragms.

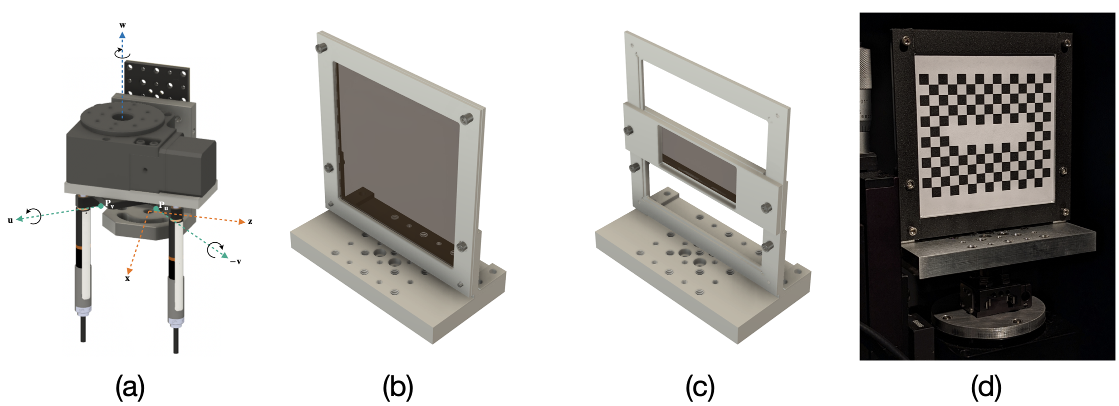

Figure 3.4: (a) Sample motion assembly without sample mount; (b) Sample mount configured for calibration target (not drawn to scale with respect to (a)); (c) Sample mount configured for scattering sample on a microscope slide (not drawn to scale with respect to (a)); (d) Sample mount shown on top of sample assembly with calibration target installed

3.1.3 Sample assembly

The sample motion assembly is primarily used to rotate the scattering sample in order to maximize the amount of laser light transmitted through the air-glass interface as the illuminators' azimuthal position changes. This rotation is controlled by a small rotation stage which is mounted on an XYZ stage and an tip/tilt stage. These additional stages are used to control the rotation stage's orientation so it can made to be collinear with the illuminator assembly's azimuthal rotation axis. There is an additional translation stage mounted to the rotation stage's motion plate that is used to align the center of a mounted sample with the upper- and lower motion stages' rotation axes.

Sample Mount

The sample mount is a custom, dual purpose mount used to hold scattering samples during acquisition and checkerboard targets during calibration. It is designed such that the front face of a calibration target is in the same plane as the central plane of a scattering sample. It consists of a base and angle mounts used to attach a square aluminum frame that holds a 10×10 cm glass window in place through compression by tightening four thumbscrews. Scattering samples are mounted by removing the aluminum frame's front face and attaching an inset frame that holds microscope slides via compression.

Chapter 4

Scatterometer Calibration and Alignment

In this chapter, we detail the scatterometer calibration and alignment processes.

4.1 Calibration and alignment

4.2 Lower Stage Calibration

The goal of calibrating the lower assembly is to estimate its rotation axis and the 3D orientation of the illumination beams as a function of the azimuth angle θ. We do so by computing the 3D intersection of each illumination beam with a series of N planes whose poses we know. This process is repeated for all

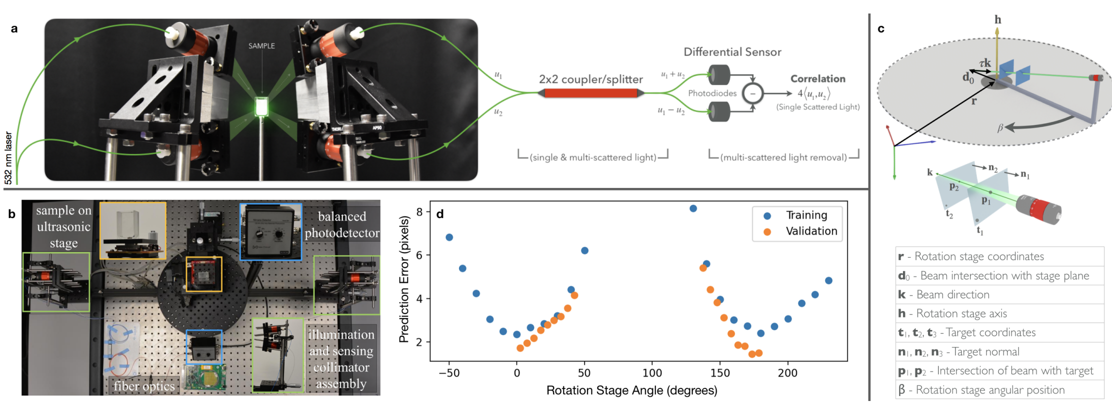

Figure 4.1: **a**: Speckle correlation computation pipeline. The sample is illuminated by two beams, and the correlation is computed using a differential sensor. **b**: Physical setup with sample placed on the circular breadboard. The illumination stand rotates about the sample while the sensing stand measures scattered light. The differential photodetector enables fast correlation computation. **c**: Geometry used to develop forward model for inverse problem estimation of 3D beam-plane intersection points. **d**: Mean estimation errors for training and validation phases showing angular dependence of error.

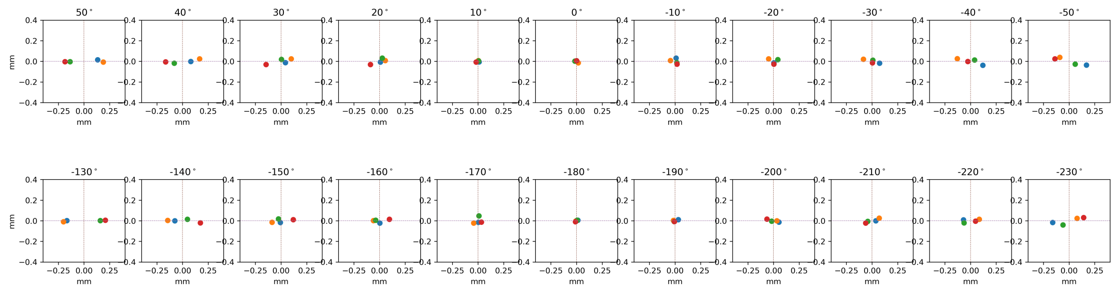

Figure 4.2: Perpendicular offsets of the four observed beam-plane intersections with respect to the estimated beam direction. Each plot is for an azimuthal angle $\theta \in \Theta$. The cause of increasing perpendicular offsets for increasing angle with respect to the plane normal and anti-normal is unknown.

$\theta \in \Theta$ for a total of $2N|\Theta|$ points. From this set of points, we can estimate the illumination directions for both beams as a function of θ and the azimuth stage pose up to a rotational ambiguity about its rotation axis.

Azimuth Stage Rotation Axis Each beam is associated with a set of $N|\Theta|$ points. Define a set of difference vectors $\{\tilde{\boldsymbol{k}}_\theta\}$, $|\{\tilde{\boldsymbol{k}}_\theta\}| = L$ as the differences between all N permute 2 points along a ray. We define a ray as a beam located at any particular $\theta \in \Theta$. Each $\tilde{\boldsymbol{k}}_\theta$ makes an angle $\pi/2 - \alpha$ with the rotation axis. However, the ${}_LP_2$ second order difference vectors are perpendicular to the azimuth rotation axis $\hat{\mathbf{h}}$, and we estimate $\hat{\mathbf{h}}$ as their null space.

Beam Direction for $\theta = 0$ Once we know the azimuth rotation axis, we can use it to estimate both illuminators' beam directions. For each $\theta \in \Theta$, we compute the centroid $\overline{\boldsymbol{p}}_\theta = \frac{1}{N}\sum p_n$. We subtract the centroid from the point set so it is zero mean and rotate it about $\hat{\mathbf{h}}$ by $-\theta$ so all points are aligned with $\theta = 0$. The beam direction $\boldsymbol{k}_0$ is simply the point set's principal component.

4.2.1 Stage Position & Beam Direction as a Function of θ

Assume a collimated beam fixed to a rotation stage with location $\boldsymbol{r}$ and rotation axis $\hat{\mathbf{h}}$. If the stage is rotated 360 degrees, the pencil of rays created by the rotated beam will form a paraboloid with axis $\hat{\mathbf{h}}$ and small radius ρ equal to the distance of closest encounter of the beam with the paraboloid axis. The locus of these points of closest encounter constitutes the beam's ray envelope. Note: Insert ray envelope theory The isoline of the ray envelope is

$$\boldsymbol{c}(\theta) = \boldsymbol{r} + \delta\hat{\mathbf{h}} + r(\theta)\boldsymbol{\rho}_0, \tag{4.1}$$

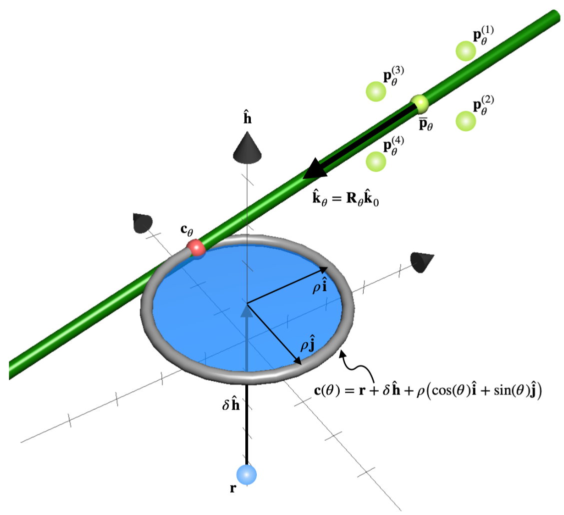

Figure 4.3: RT-5 Geometry - Frustrum top Surface

where δ is the height of the circle above the stage, $\boldsymbol{\rho}$ is a 2×1 vector. $r(\theta)$ is a 3×2 matrix consisting of a rotation of two basis vectors $\hat{\mathbf{i}}$ and $\hat{\mathbf{j}}$ through an angle of θ about the rotation axis $\hat{\mathbf{h}}$ with each basis vector being perpendicular to $\hat{\mathbf{h}}$

$$r(\theta) = \boldsymbol{R}(\hat{\mathbf{h}}, \theta) \begin{bmatrix} \hat{\mathbf{i}} & \hat{\mathbf{j}} \end{bmatrix}, \quad \boldsymbol{R}(\hat{\mathbf{h}}, \theta) \in \mathbb{R}^{3\times3}. \tag{4.2}$$

If M points $\boldsymbol{p}_\theta^{(1)}, \boldsymbol{p}_\theta^{(2)}, ..., \boldsymbol{p}_\theta^{(M)}$ are measured along the ray at a given rotation stage position $\theta \in \Theta$, then the beam with direction $\hat{\mathbf{k}}_\theta$ passes through their centroid $\overline{\boldsymbol{p}}_\theta$ with its pencil defined

$$\boldsymbol{l}_\theta(s) = \overline{\boldsymbol{p}}_\theta + s\hat{\mathbf{k}}_\theta \tag{4.3}$$

4.2.2 Azimuth Stage Location

Given the problem formulation, the objective is to find the circular conic section with perimeter $\boldsymbol{c}(\theta)$ by choosing $\boldsymbol{r}$ such that the circle's radius ρ is minimized. We achieve this by computing the minimum distance of each beam from the axis of rotation and minimizing the variance across all angles:

$$\min_{\boldsymbol{r}} g_2(\boldsymbol{r}) \tag{4.4}$$

$$\min_{\boldsymbol{r}} \sigma^2(\{\rho_\theta\}) \tag{4.5}$$

$$\min_{\boldsymbol{r}} \sum_{\theta\in\Theta} (\rho_\theta - \overline{\rho})^2 \tag{4.6}$$

where

$$\rho_\theta = \hat{\mathbf{n}}_\theta^\top(\overline{\boldsymbol{p}}_\theta - \boldsymbol{r}), \quad \hat{\mathbf{n}}_\theta = \frac{\hat{\mathbf{k}}_\theta \times \hat{\mathbf{h}}}{\|\hat{\mathbf{k}}_\theta \times \hat{\mathbf{h}}\|}, \quad \overline{\rho} = \frac{1}{|\Theta|}\sum \rho_\theta \tag{4.7}$$

We minimize the objective by computing its partial derivative with respect to $\boldsymbol{r}$. Firstly, we define

$$\overline{\boldsymbol{n}}_{\overline{\boldsymbol{p}}} = \frac{1}{|\Theta|}\sum \hat{\mathbf{n}}_\theta^\top \overline{\boldsymbol{p}}_\theta, \quad \overline{\boldsymbol{n}} = \frac{1}{|\Theta|}\sum_\theta \hat{\mathbf{n}}_\theta, \tag{4.8}$$

and compute the partial derivative with respect to $\boldsymbol{r}$:

$$\frac{\partial g_2(\boldsymbol{r})}{\partial \boldsymbol{r}} = \sum_\theta (\rho_\theta - \overline{\rho})(\overline{\boldsymbol{n}} - \hat{\mathbf{n}}_\theta) \tag{4.9}$$

$$= \sum_\theta \Big[-(\hat{\mathbf{n}}_\theta^\top \overline{\boldsymbol{p}}_\theta)\hat{\mathbf{n}}_\theta + (\hat{\mathbf{n}}_\theta^\top \boldsymbol{r})\hat{\mathbf{n}}_\theta + \overline{\boldsymbol{n}}_{\overline{\boldsymbol{p}}}\hat{\mathbf{n}}_\theta - (\overline{\boldsymbol{n}}^\top \boldsymbol{r})\hat{\mathbf{n}}_\theta + (\hat{\mathbf{n}}_\theta^\top \overline{\boldsymbol{p}}_\theta)\overline{\boldsymbol{n}} - (\hat{\mathbf{n}}_\theta^\top \boldsymbol{r})\overline{\boldsymbol{n}} - \overline{\boldsymbol{n}}_{\overline{\boldsymbol{p}}}\overline{\boldsymbol{n}} + (\overline{\boldsymbol{n}}^\top \boldsymbol{r})\overline{\boldsymbol{n}} \Big] \tag{4.10}$$

$$= \sum_\theta \Big[-(\hat{\mathbf{n}}_\theta^\top \overline{\boldsymbol{p}}_\theta)\hat{\mathbf{n}}_\theta + \overline{\boldsymbol{n}}_{\overline{\boldsymbol{p}}}\hat{\mathbf{n}}_\theta + (\hat{\mathbf{n}}_\theta^\top \overline{\boldsymbol{p}}_\theta)\overline{\boldsymbol{n}} - \overline{\boldsymbol{n}}_{\overline{\boldsymbol{p}}}\overline{\boldsymbol{n}} \Big] + \sum_\theta \Big[(\hat{\mathbf{n}}_\theta^\top \boldsymbol{r})\hat{\mathbf{n}}_\theta - (\overline{\boldsymbol{n}}^\top \boldsymbol{r})\hat{\mathbf{n}}_\theta - (\hat{\mathbf{n}}_\theta^\top \boldsymbol{r})\overline{\boldsymbol{n}} + (\overline{\boldsymbol{n}}^\top \boldsymbol{r})\overline{\boldsymbol{n}} \Big] \tag{4.11}$$

We define

$$\boldsymbol{N}_\theta = \sum_\theta \hat{\mathbf{n}}_\theta \hat{\mathbf{n}}_\theta^\top, \quad \overline{\boldsymbol{N}}_\theta = \sum_\theta \hat{\mathbf{n}}_\theta \overline{\boldsymbol{n}}^\top, \quad \overline{\boldsymbol{N}} = \sum_\theta \overline{\boldsymbol{n}}\overline{\boldsymbol{n}}^\top, \tag{4.12}$$

set the partial derivative equal to zero, and rearrange it to the form $\boldsymbol{A}\boldsymbol{x} = \boldsymbol{b}$:

$$\sum_\theta \Big[\hat{\mathbf{n}}_\theta \hat{\mathbf{n}}_\theta^\top - \hat{\mathbf{n}}_\theta \overline{\boldsymbol{n}}^\top - \overline{\boldsymbol{n}}\hat{\mathbf{n}}_\theta^\top + \overline{\boldsymbol{n}}\overline{\boldsymbol{n}}^\top \Big]\boldsymbol{r} = \sum_\theta \Big[(\hat{\mathbf{n}}_\theta^\top \overline{\boldsymbol{p}}_\theta)\hat{\mathbf{n}}_\theta - \overline{\boldsymbol{n}}_{\overline{\boldsymbol{p}}}\hat{\mathbf{n}}_\theta - (\hat{\mathbf{n}}_\theta^\top \overline{\boldsymbol{p}}_\theta)\overline{\boldsymbol{n}} + \overline{\boldsymbol{n}}_{\overline{\boldsymbol{p}}}\overline{\boldsymbol{n}} \Big] \tag{4.13}$$

$$\big(\boldsymbol{N}_\theta - \overline{\boldsymbol{N}}_\theta - \overline{\boldsymbol{N}}_\theta^\top + \overline{\boldsymbol{N}}\big)\boldsymbol{r} = \sum_\theta (\hat{\mathbf{n}}_\theta^\top \overline{\boldsymbol{p}}_\theta)\hat{\mathbf{n}}_\theta - \overline{\boldsymbol{n}}_{\overline{\boldsymbol{p}}}\sum_\theta \hat{\mathbf{n}}_\theta + \Big(-\sum_\theta \hat{\mathbf{n}}_\theta^\top \overline{\boldsymbol{p}}_\theta + \sum_\theta \overline{\boldsymbol{n}}_{\overline{\boldsymbol{p}}} \Big)\overline{\boldsymbol{n}} \tag{4.14}$$

$$\big(\boldsymbol{N}_\theta - 2\overline{\boldsymbol{N}}_\theta + \overline{\boldsymbol{N}}\big)\boldsymbol{r} = \sum_\theta (\hat{\mathbf{n}}_\theta^\top \overline{\boldsymbol{p}}_\theta)\hat{\mathbf{n}}_\theta - \overline{\boldsymbol{n}}_{\overline{\boldsymbol{p}}}|\Theta|\overline{\boldsymbol{n}} + \Big(-|\Theta|\overline{\boldsymbol{n}}_{\overline{\boldsymbol{p}}} + |\Theta|\overline{\boldsymbol{n}}_{\overline{\boldsymbol{p}}} \Big)\overline{\boldsymbol{n}} \tag{4.15}$$

$$\big(\boldsymbol{N}_\theta - 2\overline{\boldsymbol{N}}_\theta + \overline{\boldsymbol{N}}\big)\boldsymbol{r} = \sum_\theta (\hat{\mathbf{n}}_\theta^\top \overline{\boldsymbol{p}}_\theta)\hat{\mathbf{n}}_\theta - |\Theta|\overline{\boldsymbol{n}}_{\overline{\boldsymbol{p}}}\overline{\boldsymbol{n}} \tag{4.16}$$

We solve equation 4.44 with the equality constraint $\hat{\mathbf{h}}^\top(\boldsymbol{r} - \boldsymbol{t}_2) = 0$. The resulting RT-5 location $\boldsymbol{r}$ is similar to the estimate in the first method with a displacement vector norm of only 0.001 mm, and the mean distance $\overline{\rho} = 0.42$mm (as expected).

4.2.3 Ray Envelope Center

Given $\boldsymbol{r}$ and $\{\rho_\theta\}_\Theta$, a point $\boldsymbol{c}_\theta$ is defined on each ray such that its distance from the RT-5 axis is equal to ρ_θ.

$$\boldsymbol{c}_\theta = \overline{\boldsymbol{p}}_\theta + t_\theta \hat{\mathbf{k}}_\theta \tag{4.17}$$

where

$$t_\theta = \frac{\boldsymbol{m}_\theta^\top B(\boldsymbol{r} - \overline{\boldsymbol{p}}_\theta)}{\boldsymbol{m}_\theta^\top B\hat{\mathbf{k}}_\theta}, \quad \boldsymbol{m}_\theta = \hat{\mathbf{n}}_\theta \times \hat{\mathbf{k}}_\theta \tag{4.18}$$

Given the set $\{\boldsymbol{c}_\theta\}_\Theta$, we solve the following minimization problem to choose the center of the circular ray envelope $\boldsymbol{r} + \delta\hat{\mathbf{h}}$ whose radius is $\overline{\rho}_\theta$:

$$\begin{aligned} &\min_\delta g_3(\boldsymbol{r}, \delta, \boldsymbol{c}_\theta) \\ &\min_\delta \sum_{\theta\in\Theta} \left(\|\boldsymbol{c}_\theta - \boldsymbol{r} - \delta\hat{\mathbf{h}}\|^2 - \overline{\rho}^2\right)^2. \end{aligned} \tag{4.19}$$

The partial derivative with respect to δ is

$$\frac{\partial g_3(\boldsymbol{r}, \delta, \boldsymbol{c}_\theta)}{\partial\delta} = 4|\Theta|\delta^3 + 3B\delta^2 + 2C\delta + D = 0 \tag{4.20}$$

where

$$B = 4\hat{\mathbf{h}}^\top \sum(\boldsymbol{r} - \boldsymbol{c}_\theta), \quad C = 2\sum\left[2(\boldsymbol{r} - \boldsymbol{c}_\theta)^\top \hat{\mathbf{h}}\hat{\mathbf{h}}^\top(\boldsymbol{r} - \boldsymbol{c}_\theta) + \|\boldsymbol{c}_\theta\|^2 - 2\mathbf{c}_\theta^\top \boldsymbol{r} + \|\boldsymbol{r}\|^2\right], \tag{4.21}$$

$$D = 4\hat{\mathbf{h}}^\top \sum(\boldsymbol{r} - \boldsymbol{c}_\theta)(\|\boldsymbol{c}_\theta\|^2 - 2\mathbf{c}_\theta^\top \boldsymbol{r} + \|\boldsymbol{r}\|^2) \tag{4.22}$$

The partial derivative is a third degree polynomial whose roots minimize the objective function $g_3()$. We find its roots via the roots() method from the numpy.polynomial.Polynomial class.

4.2.4 Ray Envelope Isoline

We find its radius and orientation defined by the vector $\boldsymbol{\rho}_0$ such that $\boldsymbol{c}(0) = \boldsymbol{r} + \delta\hat{\mathbf{h}} + \boldsymbol{\rho}_0$ is the point on the ray envelope corresponding to azimuthal position 0°. Given $\boldsymbol{r}$ and δ, and a set of points $\{\boldsymbol{c}_\theta\}$ defined by the intersections of rays with the ray envelope plane, we can solve for the least-squares optimal $\boldsymbol{\rho}_0$ using Equation 4.35:

$$\min_{\boldsymbol{\rho}_0} \sum_\theta \|R_\theta \boldsymbol{\rho}_0 - (\boldsymbol{c} - \boldsymbol{r} - \delta\hat{\mathbf{h}})\| \tag{4.23}$$

4.2.5 Training & Validation Datasets

The training set consists of 22 rotation stage positions in 10° increments spanning ±50° relative to the normal on both faces of a target, totaling 100° and a measurement for each target. The differences of these 3D point-plane intersections are computed as the initial beam direction estimates $\overline{\mathbf{k}}$. Given a learned model, the objective is to predict point-plane intersections for new planes and angles. The similar to training but with random target positions and a smaller angular sweep. Actual phase function measurements will be constrained to a 180° range. Therefore, the validation set consists of angles within this range, each offset from training angles by 5°.

4.3 Sample Motion Assembly Calibration

The goal in calibrating the sample motion assembly is estimating the primary rotation stage's pose as well as the translation and rotation axes of all stages used to position and orient the rotation stage.

Rotation Stage Pose Estimating the rotation stage pose is similar to the method used to estimate the azimuthal rotation axis. Rather than rotating a laser and computing beam-plane intersections, we we take photos of a series of N rotated planes and detect a 3D grid of M points on each plane. ${}_NP_2$ 1st-order difference vectors are computed for each of the M points in the grid totaling $M({}_NP_2)$ vectors that are in the plane of rotation. The rotation axis $\hat{\mathbf{w}}$ is perpendicular to the plane of rotation and is therefore the null space of the vector set.

Translation Stage Axes All translation stage axes are estimated by computing 3D coordinates of checkerboard corners at several positions along the translation stage's range of motion. Difference vectors are computed for all combinations of corresponding points on the planes, and the axis is the mean of all difference vectors. The vector is oriented to point in the direction of increasing stage position.

Tip & Tilt Stage Axes The sample assembly is oriented using a 2-axis tip/tilt kinematic stage. These axes are not used in any analytical expressions; they are simply used as a 2D basis for azimuthal rotation axis PID alignment. Their limited range of motion and image noise produce unstable estimates, so visually approximated estimates are sufficient as long as the axes are perpendicular.

4.4 Aligning Sample and Illuminator Assemblies

The sample and illuminator assemblies are aligned when their rotation axes are collinear.

4.4.1 Rotation

We define a plane $\mathbf{\Pi}$ with normal vector $\hat{\mathbf{h}}$ and origin $\boldsymbol{p}_{\hat{\mathbf{h}}}$. This plane defines a basis with projection matrix $\mathbf{\Pi} \in \mathbb{R}^{2\times 3}$ whose rows are in the null space of $\hat{\mathbf{h}}$. The sample assembly's rotation axis $\hat{\mathbf{w}}$ is aligned with the azimuthal axis when its projection $\mathbf{\Pi}\hat{\mathbf{w}} = \mathbf{0}$. For PID control we seek to express the alignment error vector $\boldsymbol{\epsilon} = \mathbf{\Pi}\hat{\mathbf{w}}$ in terms of two independent error components ϵ_u and ϵ_v controlled by u- and v-axis rotation respectively. Since rotation affects motion in a plane perpendicular to the axis, and the tip and tilt axes are perpendicular, we can express the alignment errors independently by defining a new error vector $\boldsymbol{\epsilon}'$ in terms of a modified basis $\boldsymbol{\Pi}' = \boldsymbol{\Pi}[\hat{\mathbf{u}}\ \hat{\mathbf{v}}]$. The new error vector is

$$\boldsymbol{\epsilon}' = \begin{bmatrix} \epsilon'_v \\ \epsilon'_u \end{bmatrix} = \boldsymbol{\Pi}'\hat{\mathbf{w}}. \tag{4.24}$$

Note the swapped order of the elements in the error vector due to perpendicularity: the u-axis error is the projection of $\hat{\mathbf{w}}$ onto the v-axis, and the v-axis error is the projection of $\hat{\mathbf{w}}$ onto the u-axis. This modified basis preserves the mapping of zero alignment error to the zero vector.

Although the tip and tilt axes are perpendicular, they are not independent since the square motion plate is actuated at opposite corners with a shared ball joint pivot point at another. Therefore, the alignment loop alternates between the u- and v-axis PID controllers with state error updates between each controller. The stage has limited range of motion due to space constraints, so we use the Zielger-Nichols "no overshoot" gain configuration.

Translation Once the two rotation axes are parallel, we use the x- and z-axis translation stages to make the collinear.

4.5 Aligning Calibration Target with Sample Motion Assembly Rotation Axis

The compact translation stage mounted on top of the RT-3 stage is used to position the calibration target locally such that the RT-3's rotation axis intersects the calibration target's surface at the height of a scattering sample. The error is computed by first defining a horizontal line on the calibration target whose height places it approximately midway along the height of a scattering sample. Define the minimum-length displacement vector between the two axes as $\boldsymbol{\delta}$. The error is then the projection of $\boldsymbol{\delta}$ onto the stage's translation axis $\boldsymbol{m}$.

Define the mean beam direction vector $\overline{\boldsymbol{k}} = (\hat{\mathbf{k}}_0^{(a)} + \hat{\mathbf{k}}_0^{(b)})/2$. For target with plane normal $\hat{\mathbf{z}}$, the objective is

$$\min_{\psi} 1 - \overline{\boldsymbol{k}}^{\mathsf{T}}\hat{\mathbf{z}}(\psi) \tag{4.25}$$

where $\hat{\mathbf{z}}(\psi) = \boldsymbol{R}_{\hat{\mathbf{w}}}\hat{\mathbf{z}}_0$ is the initial normal vector rotated about $\hat{\mathbf{w}}$ by an angle ψ.

Two points $\boldsymbol{P}_1, \boldsymbol{P}_2$ on plane Π_a with corresponding image points $\boldsymbol{p}_1, \boldsymbol{p}_2 \in \mathbb{P}^2$ create the line $\boldsymbol{\ell} = \boldsymbol{p}_1 \times \boldsymbol{p}_2$. We write the Euclidean intersection of the $\boldsymbol{w}$ axis with plane Π_a as $\boldsymbol{P}_i = \boldsymbol{P}_{w'} + \gamma_{\Pi_b}\hat{\mathbf{w}}$ where Π_b: kernel$(\boldsymbol{P}_1, \boldsymbol{P}_2, \boldsymbol{P}_3)$ s.t. $\measuredangle(\Pi_a, \Pi_b) = \pi/4$. Goal: Adjust compact stage position such that $\boldsymbol{P}_i$ lies on $\boldsymbol{\ell}$. This is true when $\boldsymbol{p}_i^{\mathsf{T}}\boldsymbol{\ell} = 0$ in the image frame.

$$\hat{\mathbf{z}}' = \frac{(\boldsymbol{P}_2 - \boldsymbol{P}_1) \times (\boldsymbol{P}_3 - \boldsymbol{P}_1)}{\|(\boldsymbol{P}_2 - \boldsymbol{P}_1) \times (\boldsymbol{P}_3 - \boldsymbol{P}_1)\|} \tag{4.26}$$

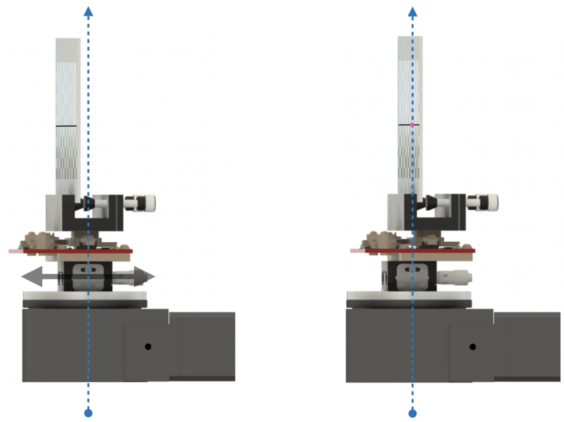

Figure 4.4: Sample motion assembly without sample mount

$$\boldsymbol{p}_i = \tau \boldsymbol{M}\left((\boldsymbol{\alpha}^\intercal \hat{\mathbf{z}}')\delta + \hat{\mathbf{w}}(\boldsymbol{P}_1 - \boldsymbol{P}_{w'})^\intercal \hat{\mathbf{z}}' + \frac{1}{\tau}\boldsymbol{P}_{w'} \right) \tag{4.27}$$

where $\boldsymbol{M}$ is the camera projection matrix, and $\tau = (\boldsymbol{w}^\intercal \hat{\mathbf{z}}')^{-1}$

$$\boldsymbol{\ell} = \boldsymbol{M}\Big((\boldsymbol{\alpha} \times \boldsymbol{P}_2 + \boldsymbol{P}_1 \times \boldsymbol{\alpha})\delta + \boldsymbol{P}_1 \times \boldsymbol{P}_2 \Big) \tag{4.28}$$

The signed error is

$$\epsilon = \boldsymbol{p}_i^\intercal \boldsymbol{\ell} \tag{4.29}$$

4.6 Aligning Sample Motion Assembly and Illumination Beams

The objectives for beam alignment are to orient the two laser beams such that 1) their intersection point is located on the RT-3 and RT-5 rotation axes, 2) their mean direction is perpendicular to the rotation axis, and 3) they are normal to the calibration target's surface. We will consider the upper and lower stages' axes collinear, and alignment will be discussed with respect to the azimuthal axis of the lower stage assembly.

$$\ell = 2\frac{d_0}{\sin\theta}\cos\theta/2 \tag{4.30}$$

$$d = 2\frac{d_0}{\sin\theta}\sin\theta/2 \tag{4.31}$$

Beams equianglular with respect to RT-3 and RT-5 axes The mean direction is perpendicular to the rotation axis when both beams' projections onto the azimuthal axis are equal and opposite:

$$0 = \hat{\mathbf{k}}_a^\intercal \boldsymbol{h} + \hat{\mathbf{k}}_b^\intercal \boldsymbol{h}. \tag{4.32}$$

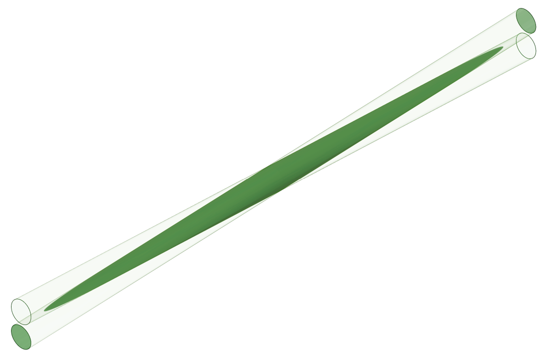

Figure 4.5

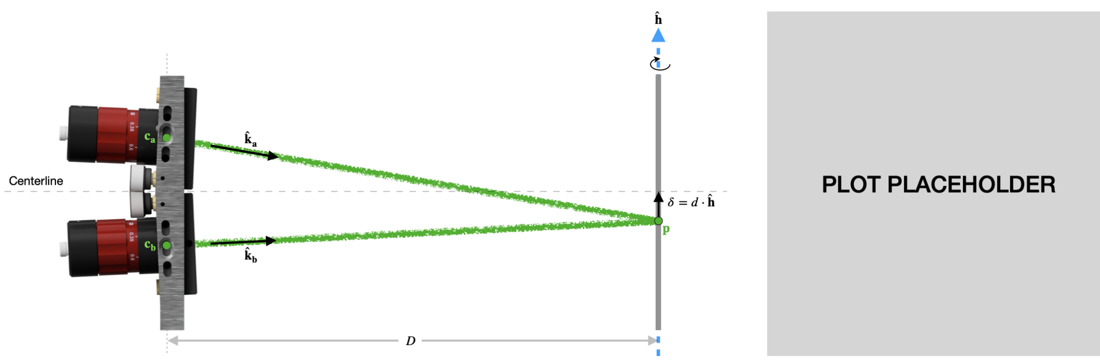

Figure 4.6

Define both collimators' positions $\boldsymbol{c}_a, \boldsymbol{c}_b$, and assume both beams intersect at point $\boldsymbol{p}$ on the azimuthal axis. The ideal intersection point $\boldsymbol{p}^*$ is located at the intersection of the collimators' horizontal plane of symmetry and the azimuthal axis. $\boldsymbol{p}$ is offset from the ideal intersection point by displacement vector $\boldsymbol{\delta} = \boldsymbol{p}^* - \boldsymbol{p} = d \cdot \boldsymbol{h}$. Equation 4.32 can be rewritten in terms of these variables to solve for the displacement distance d along $\hat{\mathbf{h}}$:

$$
\begin{aligned}
0 &= (\boldsymbol{p} + \boldsymbol{\delta} - \boldsymbol{c}_a)^\top \boldsymbol{h} + (\boldsymbol{p} + \boldsymbol{\delta} - \boldsymbol{c}_b)^\top \boldsymbol{h} \\
2\boldsymbol{\delta}^\top \boldsymbol{h} &= (\boldsymbol{c}_a - \boldsymbol{p})^\top \boldsymbol{h} + (\boldsymbol{c}_b - \boldsymbol{p})^\top \boldsymbol{h} \\
2\boldsymbol{\delta}^\top \boldsymbol{h} &= (\boldsymbol{c}_a - \boldsymbol{p} + \boldsymbol{c}_b - \boldsymbol{p})^\top \boldsymbol{h} \\
d \cdot \boldsymbol{h}^\top \boldsymbol{h} &= \tfrac{1}{2} (\boldsymbol{c}_a - \boldsymbol{p} + \boldsymbol{c}_b - \boldsymbol{p})^\top \boldsymbol{h} \\
d &= \tfrac{1}{2} \left[(\boldsymbol{c}_a - \boldsymbol{p}) + (\boldsymbol{c}_b - \boldsymbol{p}) \right]^\top \boldsymbol{h}
\end{aligned}
\tag{4.33}
$$

The displacement vectors $\boldsymbol{c}_a - \boldsymbol{p}$ and $\boldsymbol{c}_b - \boldsymbol{p}$ are unknown since the collimator positions are unknown. However, the normalized beam directions $\hat{\mathbf{k}}_a, \hat{\mathbf{k}}_b$ are parallel to these displacement vectors, so we use

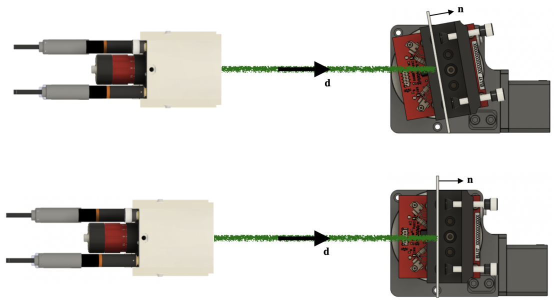

Figure 4.7: Top: Target and beam misaligned due to non-zero angle between the beam and the target normal; Bottom: $\boldsymbol{d}$ aligned with normal vector $\boldsymbol{n}$. Note: Update by replacing d with kbar.

a scalar coefficient s to achieve the correct scale. We determine s using the CAD model based on the nominal design geometry, and the final beam intersection displacement expression is

$$d = -\frac{s}{2}(\hat{\mathbf{k}}_a + \hat{\mathbf{k}}_b)^\top \boldsymbol{h}. \tag{4.34}$$

The alignment procedure is as follows. Since the beams' orientations have been adjusted since their initial estimation, we begin by updating their estimates. We use a method similar to that detailed in section 4.2, but we make measurements at a single azimuthal position $\theta = 0$. With updated $\hat{\mathbf{k}}_a$ and $\hat{\mathbf{k}}_b$, we compute the required intersection point displacement via Equation 4.34. The displacement is projected into the image frame, and the beams are commanded to the corresponding pixel backprojected to the calibration target. This process is repeated iteratively until the displacement distance is below a threshold due to inaccuracies introduced by the rough estimate of the scale factor s and other noise sources.

4.7 Aligning Calibration Target with Illumination Beams

This alignment step determines the "home" position of the sample assembly's rotation stage which corresponds to sample illumination along its normal vector. The home position maximizes the inner product of the target's normal vector and the mean illumination beam vector $\overline{\boldsymbol{k}} = (\hat{\mathbf{k}}_a + \hat{\mathbf{k}}_b)/2$.

4.8 Note: Proposal:Acquisition Camera Calibration

The projection matrix can be estimated via PnP in theory. However, we found it challenging in practice due to 3D points at infinity providing no depth information, and the geometry of a camera focused at infinity producing unstable estimates due to an effective coupling of the intrinsic parameters. Note: Add reasons they fail. Since the acquisition camera maps points from the plane at infinity to the image plane,

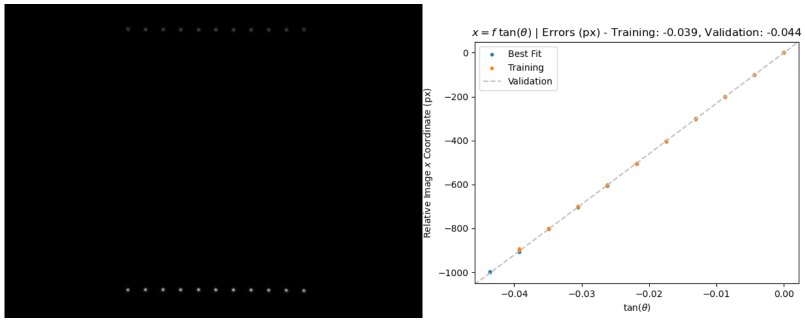

Figure 4.8: Left: Composite of 11 images of both illuminators spanning an azimuth range 3.5°. Right: The acquisition camera's focal length is the constant of proportionality of image point displacement and the tangent of the internal ray angle with respect to the optical axis.

the homography for these planes is the projection matrix. However, there is an effective coupling of intrinsic parameters that complicates decomposing the projection matrix into a product of intrinsic and extrinsic matrices.

A camera focused at infinity maps rays along its optical axis to its principal point; all directions measured relative to the optical axis are mapped to image points relative to the principal point. Translating the principal point is similar to rotating the camera externally under the small angle approximation $\tan(\phi) \approx \phi$. Therefore, these two parameters are effectively coupled for a non-WFOV camera. Note: Insert figure showing reprojection error loss vs. pp and rotation. To avoid this issue, we estimate the focal length using a simple geometric relationship describing pinhole cameras focused at infinity followed principal point estimation via inspection. Once the intrinsics are known, we estimate the rotation matrix and the lens distortion coefficients simultaneously.

4.8.1 Intrinsics

Rays entering the camera at an angle ϕ with respect to the optical axis are mapped to a point $f_{px} \tan(\phi)$ pixels from the principal point. This relation can be used to estimate the focal length given a set of rays with known directions and their corresponding image pixel coordinates. Since beam directions are known for all azimuth angles from lower stage calibration Note: Insert reference, we acquire images of beams rotated azimuthally, we compute the ray angle with respect to the optical axis and the pixel spacing. If we plot the pixel spacing vs. the tangent of the local ray angle, the line of best fit has a slope equal to the equivalent pinhole's focal length. We estimate the principal point by shining a collimated source into the lens oriented so it is approximately parallel to the lens' optical axis. The location of its image is assumed to be the principal point.

4.8.2 Extrinsics & Lens Distortion

Note: Newton-Raphson method via pytorch-minimize.

4.8.3 Validation

The calibration model is validated on the physical acquisition system by learning a model on training data and then evaluating performance via a validation dataset. First, a checkerboard calibration target is placed at two different locations, and its poses are determined using a calibrated camera. A laser is attached to a rotation stage, and an image of the beam spot on the target is acquired at each position. The 3D beam-plane intersection point is then calculated using beam spot centroiding to find the pixel coordinates which are backprojected to the camera's frame using the camera matrix. The rotation stage axis $\mathbf{h}$ is determined by placing a target face-up on the stage and estimating the target's normal with the camera.

Validation Results Figure 4.1d shows the training and validation estimation errors of 3D points. Angles less than 90° correspond to the target illuminated from the front with 0° corresponding to Figure 4.1c. Those to the right correspond to a back-illuminated target with 180° being anti-normal. The training and validation errors have similar trends with reduced validation error, suggesting the data was not over-fit. There is no error benchmark rooted in a performance metric. However, since centroiding and the homography computed during calibration both have sub-pixel accuracy and this is ultimately an interpolation task, the targeted prediction accuracy is sub-pixel. Considering the minimum validation error is 1.5 pixels with a mean error of 2.8 pixels, the targeted accuracy seems achievable if the issue of worsening error with angle of incidence is alleviated and the beam direction estimates are improved.

4.9 Note: Proposal:Illuminator Assembly Calibration

The goal for calibrating the illuminator assembly is estimating its rotation axis and the 3D orientation of the illumination beams as a function of the azimuth angle θ. We do so by computing the 3D intersection of each illumination beam with a series of N planes whose poses we know. This process is repeated for all $\theta \in \Theta$ for a total of $2N|\Theta|$ points. From this point set, we can estimate illumination directions for both beams as a function of θ and the azimuth stage pose up to a rotational ambiguity about its rotation axis.

Note: Proposal:Azimuth Stage Rotation Axis Each beam is associated with a set of $N|\Theta|$ points. Define a set of difference vectors $\{\tilde{\boldsymbol{k}}_\theta\},\ |\{\tilde{\boldsymbol{k}}_\theta\}| = L$ as the differences between all N permute 2 points

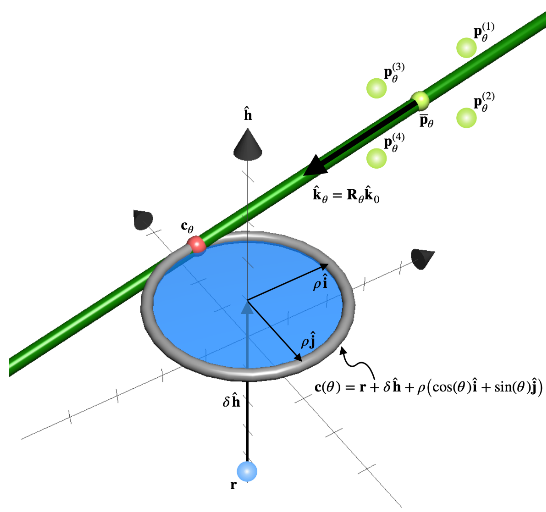

Figure 4.9: Ray envelope defined as the locus of points of closest encounter between the illumination beam and its rotation axis

along a ray. We define a ray as a beam located at any particular $\theta \in \Theta$. Each $\tilde{\boldsymbol{k}}_\theta$ makes an angle $\pi/2 - \alpha$ with the rotation axis. However, the ${}_L P_2$ 2nd order difference vectors are perpendicular to the azimuth rotation axis $\hat{\mathbf{h}}$, and we estimate $\hat{\mathbf{h}}$ as their null space.

Note: Proposal:Beam Direction Vector Once we know the azimuth rotation axis, we can use it to estimate both illuminators' beam directions. For each $\theta \in \Theta$, we compute the centroid $\overline{\boldsymbol{p}}_\theta = \frac{1}{N}\sum p_n$. We subtract the centroid from the point set so it is zero mean, and we rotate it about $\hat{\mathbf{h}}$ by $-\theta$ so all points are aligned with $\theta = 0$. The beam direction $\boldsymbol{k}_0$ is simply the point set's principal component. For any arbitrary azimuthal angle θ, we can compute the beam direction $\boldsymbol{k}_0 = \boldsymbol{R}_{\hat{\mathbf{h}}}\boldsymbol{k}_0$ where $\boldsymbol{R}_{\hat{\mathbf{h}}}$ is a 3×3 rotation matrix with azimuthal axis $\hat{\mathbf{h}}$.

4.9.1 Note: Proposal:Stage Position & Beam Direction as a Function of θ

Assume a collimated beam fixed to a rotation stage with location $\boldsymbol{r}$ and rotation axis $\hat{\mathbf{h}}$. If the stage is rotated 360 degrees, the pencil of rays created by the rotated beam will form a paraboloid with axis $\hat{\mathbf{h}}$ and small radius ρ equal to the distance of closest encounter of the beam with the paraboloid axis. The locus of these points of closest encounter constitute the beam's ray envelope. The isoline of the ray envelope is

$$\boldsymbol{c}(\theta) = \boldsymbol{r} + \delta\hat{\mathbf{h}} + r(\theta)\boldsymbol{\rho}_0, \tag{4.35}$$

where δ is the height of the circle above the stage, $\boldsymbol{\rho}$ is a 2×1 vector. $r(\theta)$ is a 3×2 matrix consisting of a rotation of two basis vectors $\hat{\mathbf{i}}$ and $\hat{\mathbf{j}}$ through an angle of θ about the rotation axis $\hat{\mathbf{h}}$ with each basis vector being perpendicular to $\hat{\mathbf{h}}$

$$r(\theta) = \boldsymbol{R}(\hat{\mathbf{h}}, \theta) \begin{bmatrix} \hat{\mathbf{i}} & \hat{\mathbf{j}} \end{bmatrix}, \quad \boldsymbol{R}(\hat{\mathbf{h}}, \theta) \in \mathbb{R}^{3\times 3}. \tag{4.36}$$

If M points $\boldsymbol{p}_\theta^{(1)}, \boldsymbol{p}_\theta^{(2)}, ..., \boldsymbol{p}_\theta^{(M)}$ are measured along the ray at a given rotation stage position $\theta \in \Theta$, then the beam with direction $\hat{\mathbf{k}}_\theta$ passes through their centroid $\overline{\boldsymbol{p}}_\theta$ with its pencil defined

$$\boldsymbol{l}_\theta(s) = \overline{\boldsymbol{p}}_\theta + s\hat{\mathbf{k}}_\theta \tag{4.37}$$

4.9.2 Note: Proposal:Azimuth Stage Location

Given the problem formulation, the objective is to find the circular conic section with perimeter $\boldsymbol{c}(\theta)$ by choosing $\boldsymbol{r}$ such that the circle's radius ρ is minimized. We achieve this by computing the minimum distance of each beam from the axis of rotation and minimizing the variance across all angles:

$$\min_{\boldsymbol{r}} \sum_{\theta\in\Theta} (\rho_\theta - \overline{\rho})^2 \tag{4.38}$$

where

$$\rho_\theta = \hat{\mathbf{n}}_\theta^\intercal (\overline{\boldsymbol{p}}_\theta - \boldsymbol{r}), \quad \hat{\mathbf{n}}_\theta = \frac{\hat{\mathbf{k}}_\theta \times \hat{\mathbf{h}}}{||\hat{\mathbf{k}}_\theta \times \hat{\mathbf{h}}||}, \quad \overline{\rho} = \frac{1}{|\Theta|} \sum \rho_\theta \tag{4.39}$$

We minimize the objective by computing its partial derivative with respect to $\boldsymbol{r}$. Firstly we define

$$\overline{\boldsymbol{n}}_{\overline{\boldsymbol{p}}} = \frac{1}{|\Theta|} \sum \hat{\mathbf{n}}_\theta^\intercal \overline{\boldsymbol{p}}_\theta, \quad \overline{\boldsymbol{n}} = \frac{1}{|\Theta|} \sum_\theta \hat{\mathbf{n}}_\theta, \tag{4.40}$$

and compute the partial derivative with respect to $\boldsymbol{r}$:

$$\frac{\partial g_2(\boldsymbol{r})}{\partial \boldsymbol{r}} = \sum_\theta (\rho_\theta - \overline{\rho})(\overline{\boldsymbol{n}} - \hat{\mathbf{n}}_\theta) \tag{4.41}$$

$$= \sum_\theta \Big[-(\hat{\mathbf{n}}_\theta^\intercal \overline{\boldsymbol{p}}_\theta)\hat{\mathbf{n}}_\theta + \overline{\boldsymbol{n}}_{\overline{\boldsymbol{p}}}\hat{\mathbf{n}}_\theta + (\hat{\mathbf{n}}_\theta^\intercal \overline{\boldsymbol{p}}_\theta)\overline{\boldsymbol{n}} - \overline{\boldsymbol{n}}_{\overline{\boldsymbol{p}}}\overline{\boldsymbol{n}} \Big] + \sum_\theta \Big[(\hat{\mathbf{n}}_\theta^\intercal \boldsymbol{r})\hat{\mathbf{n}}_\theta - (\overline{\boldsymbol{n}}^\intercal \boldsymbol{r})\hat{\mathbf{n}}_\theta - (\hat{\mathbf{n}}_\theta^\intercal \boldsymbol{r})\overline{\boldsymbol{n}} + (\overline{\boldsymbol{n}}^\intercal \boldsymbol{r})\overline{\boldsymbol{n}} \Big] \tag{4.42}$$

We define

$$\boldsymbol{N}_\theta = \sum_\theta \hat{\mathbf{n}}_\theta \hat{\mathbf{n}}_\theta^\intercal, \quad \overline{\boldsymbol{N}}_\theta = \sum_\theta \hat{\mathbf{n}}_\theta \overline{\boldsymbol{n}}^\intercal, \quad \overline{\boldsymbol{N}} = \sum_\theta \overline{\boldsymbol{n}}\overline{\boldsymbol{n}}^\intercal, \tag{4.43}$$

set the partial derivative equal to zero, and rearrange it to the form $\boldsymbol{Ax} = \boldsymbol{b}$:

$$\left(\boldsymbol{N}_\theta - 2\overline{\boldsymbol{N}}_\theta + \overline{\boldsymbol{N}}\right)\boldsymbol{r} = \sum_\theta (\hat{\mathbf{n}}_\theta^\intercal \overline{\boldsymbol{p}}_\theta)\hat{\mathbf{n}}_\theta - |\Theta|\overline{\boldsymbol{n}}_{\overline{\boldsymbol{p}}}\overline{\boldsymbol{n}} \tag{4.44}$$

We solve equation 4.44 with the equality constraint $\hat{\mathbf{h}}^\intercal (\boldsymbol{r} - \boldsymbol{t}_2) = 0$. The resulting RT-5 location $\boldsymbol{r}$ is similar to the estimate in the first method with a displacement vector norm of only 0.001 mm, and the mean distance $\overline{\rho} = 0.42$mm (as expected).

4.9.3 Note: Proposal:Ray Envelope Center

Given $\boldsymbol{r}$ and $\{\rho_\theta\}_\Theta$, a point $\boldsymbol{c}_\theta$ is defined on each ray such that its distance from the RT-5 axis is equal to ρ_θ.

$$\boldsymbol{c}_\theta = \overline{\boldsymbol{p}}_\theta + t_\theta \hat{\mathbf{k}}_\theta \tag{4.45}$$

where

$$t_\theta = \frac{\boldsymbol{m}_\theta^\top B(\boldsymbol{r} - \overline{\boldsymbol{p}}_\theta)}{\boldsymbol{m}_\theta^\top B\hat{\mathbf{k}}_\theta}, \quad \boldsymbol{m}_\theta = \hat{\mathbf{n}}_\theta \times \hat{\mathbf{k}}_\theta \tag{4.46}$$

Given the set $\{\boldsymbol{c}_\theta\}_\Theta$, we solve the following minimization problem to find the optimal center of the circular ray envelope $\boldsymbol{r} + \delta\hat{\mathbf{h}}$ whose radius is $\overline{\rho}_\theta$ and minimizes the sum of the squared distances of points from the circle:

$$\begin{aligned} &\min_\delta g_3(\boldsymbol{r}, \delta, \boldsymbol{c}_\theta) \\ &\min_\delta \sum_{\theta\in\Theta} \left(\|\boldsymbol{c}_\theta - \boldsymbol{r} - \delta\hat{\mathbf{h}}\|^2 - \overline{\rho}^2\right)^2. \end{aligned} \tag{4.47}$$

The partial derivative with respect to δ is

$$\frac{\partial g_3(\boldsymbol{r}, \delta, \boldsymbol{c}_\theta)}{\partial \delta} = 4|\Theta|\delta^3 + 3B\delta^2 + 2C\delta + D = 0 \tag{4.48}$$

where

$$B = 4\hat{\mathbf{h}}^\top \sum(\boldsymbol{r} - \boldsymbol{c}_\theta), \quad C = 2\sum\left[2(\boldsymbol{r} - \boldsymbol{c}_\theta)^\top \hat{\mathbf{h}}\hat{\mathbf{h}}^\top(\boldsymbol{r} - \boldsymbol{c}_\theta) + \|\boldsymbol{c}_\theta\|^2 - 2\mathbf{c}_\theta^\top \boldsymbol{r} + \|\boldsymbol{r}\|^2\right], \tag{4.49}$$

$$D = 4\hat{\mathbf{h}}^\top \sum(\boldsymbol{r} - \boldsymbol{c}_\theta)(\|\boldsymbol{c}_\theta\|^2 - 2\mathbf{c}_\theta^\top \boldsymbol{r} + \|\boldsymbol{r}\|^2). \tag{4.50}$$

The partial derivative is a third degree polynomial whose roots minimize the objective function $g_3(\boldsymbol{r}, \delta, \boldsymbol{c}_\theta)$.

4.9.4 Note: Proposal:Ray Envelope Isoline

We find its radius and orientation defined by the vector $\boldsymbol{\rho}_0$ such that $\boldsymbol{c}(0) = \boldsymbol{r} + \delta\hat{\mathbf{h}} + \boldsymbol{\rho}_0$ is the point on the ray envelope corresponding to azimuthal position 0°. Given $\boldsymbol{r}$ and δ, and a set of points $\{\boldsymbol{c}_\theta\}$ defined by the intersections of rays with the ray envelope plane, we can solve for the least-squares optimal $\boldsymbol{\rho}_0$ using Equation 4.35:

$$\min_{\boldsymbol{\rho}_0} \sum_\theta \|\boldsymbol{R}_\theta \boldsymbol{\rho}_0 - (\boldsymbol{c} - \boldsymbol{r} - \delta\hat{\mathbf{h}})\|. \tag{4.51}$$

4.10 Acquisition Camera Calibration

The projection matrix can be estimated using PnP in theory. However, we found it challenging in practice due to 3-D points at infinity providing no depth information, resulting in unstable estimation. Since the acquisition camera maps points from the plane at infinity to the image plane, the homography relating these planes is the projection matrix. However, there is an effective coupling of intrinsic and extrinsic parameters that complicates decomposing the projection matrix into a product of intrinsic and extrinsic matrices.

A camera focused at infinity maps rays parallel to its optical axis to its principal point; all directions measured relative to the optical axis are mapped to image points relative to the principal point. If p is the distance of a pixel from the principal point of a camera with focal length f, then $p = f\tan(\phi)$ for an incoming ray at angle θ with respect to the optical axis. Under the small angle approximation, $p \approx f\phi$ which means the pixel distance change proportionally to the incoming ray angle. Therefore, shifting the principal point is analogous to rotating the camera externally for small angles, and these two parameters are effectively coupled for a non-WFOV camera. This numerical coupling results in a reprojection error loss topology that is not strictly convex as shown in Figure 4.10(c). Therefore, we estimate the intrinsics by computing the focal length as the ambiguity's constant of proportionality and choosing a principal point. Once the intrinsics are known, we estimate the rotation matrix and the lens distortion coefficients simultaneously.

Since the focal length is the constant of proportionality for beam angle and image pixel displacement and the beam directions are known for all azimuth angles from illuminator assembly calibration, we can compute the focal length. We acquire images of the two illumination beams rotated azimuthally and compute ray angles with respect to the optical axis. If we plot the pixel spacing vs. the tangent of the local ray angle, the line of best fit has a slope equal to the equivalent pinhole camera's focal length (Figure 4.10(a,b). We separately estimate the principal point by shining a collimated source into the lens oriented so it is approximately parallel to the lens' optical axis. The location of its image is assumed to be the principal point. Finally, we estimate the camera's rotation matrix and lens distortion coefficients numerically as the parameters that minimize the reprojection error given the previously determined focal length and principal point.

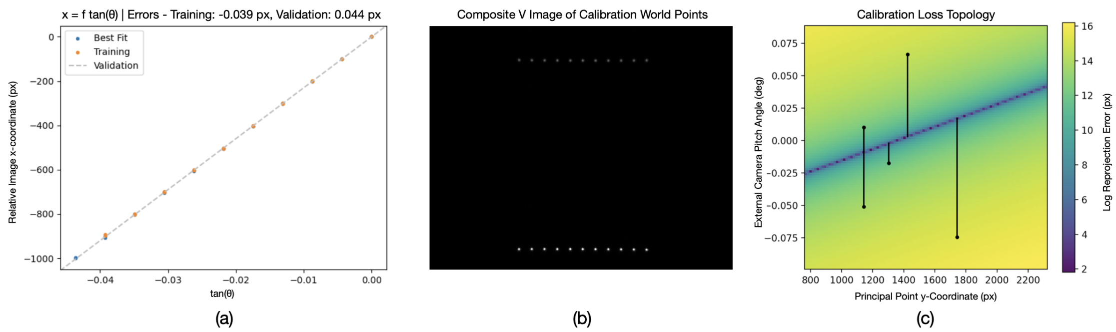

Figure 4.10: (a) The acquisition camera's focal length is the constant of proportionality of image point displacement and the tangent of the internal ray angle with respect to the optical axis; (b) Composite of 11 images of both illuminators spanning an azimuth range 3.5°; (c) Reprojection error as a function of principal point shifts along the y-axis and external pitch rotation is not strictly convex, showing the numerical ambiguity of principal point shifting and camera rotation. This ambiguity holds for the x-axis and panning as well.

4.11 Note: Proposal:Acquisition Light Efficiency

Given a linearly polarized illumination laser beam, an acquisition sensor offset by a scattering angle θ, and a scattering sample inside a glass cell, the goal is to determine 1) the optimal sample orientation and 2) the optimal angle of polarization to maximize light transmitted from the illuminator to the acquisition sensor. All theory below assumes scattering particles are small compared with the wavelength and are detailed in [7].

Note: Proposal:Fresnel Formulae

Consider a plane wave with amplitude A incident on a surface. The electric and magnetic field vectors can be decomposed into two components parallel and perpendicular to the surface plane. The incident electric field is

$$E^{(i)} = \begin{bmatrix} -A_{||} \cos\theta_i e^{-i\tau_i} \\ A_{\perp} e^{-i\tau_i} \\ A_{||} \sin\theta_i e^{-i\tau_i} \end{bmatrix} \tag{4.52}$$

where E_x, E_z are in the plane, E_y is along the plane normal, and the complex exponential argument is defined

$$\tau_i = \omega\big(t - \tfrac{\mathbf{r}^\intercal \mathbf{s}^{(i)}}{v}\big) = \omega\big(t - \tfrac{x \sin\theta_i + z\cos\theta_i}{v}\big). \tag{4.53}$$

The magnetic field vector H is written similarly through the relation $H = \sqrt{\epsilon}\mathbf{s} \times \mathbf{E}$. where $\mathbf{s}$ is the light's velocity vector. If T and R denote the transmitted and reflected amplitudes, then the transmitted field is

$$E^{(t)} = \begin{bmatrix} -T_{||} \cos\theta_t e^{-i\tau_t} \\ T_{\perp} e^{-i\tau_t} \\ T_{||} \sin\theta_t e^{-i\tau_t} \end{bmatrix}, \tag{4.54}$$

and the reflected field is

$$E^{(r)} = \begin{bmatrix} -R_{||} \cos\theta_r e^{-i\tau_r} \\ R_{\perp} e^{-i\tau_r} \\ R_{||} \sin\theta_r e^{-i\tau_r} \end{bmatrix}. \tag{4.55}$$

The tangential components of the electric and magnetic fields must be continuous across the boundary, resulting in four boundary conditions:

$$E_x^{(i)} + E_x^{(r)} = E_x^{(t)} \quad E_y^{(i)} + E_y^{(r)} = E_y^{(t)} \tag{4.56}$$

$$H_x^{(i)} + H_x^{(r)} = H_x^{(t)} \quad H_y^{(i)} + H_y^{(r)} = H_y^{(t)}. \tag{4.57}$$

These boundary conditions can be solved for an expression of the transmitted and reflected amplitudes components by using the Maxwell relation $n = \sqrt{\epsilon}$

$$T_{||} = \frac{2n_1 \cos\theta_i}{n_2 \cos\theta_i + n_1 \cos\theta_t} A_{||} \quad T_{\perp} = \frac{2n_1 \cos\theta_i}{n_1 \cos\theta_i + n_2 \cos\theta_t} A_{\perp} \tag{4.58}$$

$$R_{||} = \frac{n_2 \cos\theta_i - n_1 \cos\theta_t}{n_2 \cos\theta_i + n_1 \cos\theta_t} A_{||} \quad R_{\perp} = \frac{n_1 \cos\theta_i - n_2 \cos\theta_t}{n_1 \cos\theta_i + n_2 \cos\theta_t} A_{\perp}. \tag{4.59}$$

Note: Proposal:Effects of Polarization on Fresnel Formulae

The light intensity is

$$S = \frac{c}{4\pi} \sqrt{\epsilon} E^2 = \frac{cn}{4\pi} E^2 \tag{4.60}$$

The resulting energy incident on a surface with unit area A is

$$J^{(i)} = S^{(i)} \cos\theta_i = \frac{cn_1}{4\pi} |A|^2 \cos\theta_i \tag{4.61}$$

with reflected and transmitted energies

$$J^{(r)} = \frac{cn_1}{4\pi} |R|^2 \cos\theta_i \quad and \quad J^{(t)} = \frac{cn_2}{4\pi} |T|^2 \cos\theta_t. \tag{4.62}$$

The reflectivity and transmissivity are

$$\mathcal{R} = \frac{J^{(r)}}{J^{(i)}} = \frac{|R|^2}{|A|^2} \quad and \quad \mathcal{T} = \frac{J^{(t)}}{J^{(i)}} = \frac{|T|^2}{|A|^2} \tag{4.63}$$

which satisfy the law of conservation of energy by summing to 1

$$\mathcal{R} + \mathcal{T} = 1. \tag{4.64}$$

The reflectivity and transmissivity are functions of polarization with respect to the parallel and perpendicular directions. If the incident electric field **E** makes an angle α_i with respect to the plane, the parallel and perpendicular area components are

$$A_{||} = A\cos\alpha_i \quad \textit{and} \quad A_{\perp} = A\sin\alpha_i \tag{4.65}$$

The parallel energy component of the incident light is

$$\begin{aligned} J_{||}^{(i)} &= \frac{cn_1}{4\pi}|A_{||}|^2\cos\theta_i \\ &= \frac{cn_1}{4\pi}|A|^2\cos^2\alpha_i\cos\theta_i \\ &= J^{(i)}\cos^2\alpha_i \end{aligned} \tag{4.66}$$

with that of the perpendicular component following similarly:

$$J_{\perp}^{(i)} = J^{(i)}\sin^2\alpha_i. \tag{4.67}$$

The reflectivity in terms of polarized light is

$$\begin{aligned} \mathcal{R} = \frac{J^{(r)}}{J^{(i)}} &= \frac{J_{||}^{(r)} + J_{\perp}^{(r)}}{J^{(i)}} \\ &= \frac{J_{||}^{(r)}}{J_{||}^{(i)}}\cos^2\alpha_i + \frac{J_{\perp}^{(r)}}{J_{\perp}^{(i)}}\sin^2\alpha_i \\ &= \mathcal{R}_{||}\cos^2\alpha_i + \mathcal{R}_{\perp}\sin^2\alpha_i, \end{aligned} \tag{4.68}$$

and the transmissivity is

$$\mathcal{T} = \mathcal{T}_{||}\cos^2\alpha_i + \mathcal{T}_{\perp}\sin^2\alpha_i. \tag{4.69}$$

Reflectivity and transmissivity must satisfy conservation of energy respectively:

$$\mathcal{R}_{||} + \mathcal{T}_{||} = 1, \qquad \mathcal{R}_{\perp} + \mathcal{T}_{\perp} = 1. \tag{4.70}$$

When light is incident normal to the surface, $\alpha_i = 0$ for all E-field orientations, meaning there is no distinction between the parallel and perpendicular components, and the reflectivity and transmissivity are written

$$\mathcal{R} = \left(\frac{n-1}{n+1}\right)^2, \qquad \mathcal{T} = \frac{4n}{(n+1)^2} \tag{4.71}$$

where $n = n_2/n_1$.

These relations were used to find the optimal sample assembly rotation angle and the angle of polarization for every acquisition scattering angle. The result is a lookup table plotted as a chart in Figure 5.2.

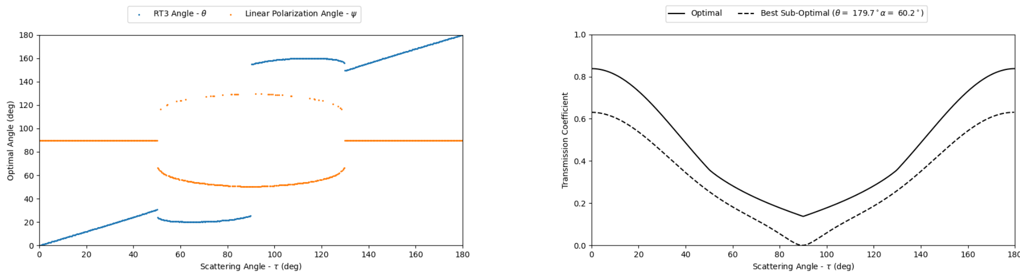

Figure 4.11: Left: Optimal sample rotation stage position and linear polarization angle as a function of azimuthal illumination angle. The linear polarization angle schedule contains discontinuities in the range $(-50°, 50°)$ due to rounding errors; Right: Comparison of light transmitted towards camera when choosing the optimal sample orientation versus a static sample shows an approximate 15% increase on average.

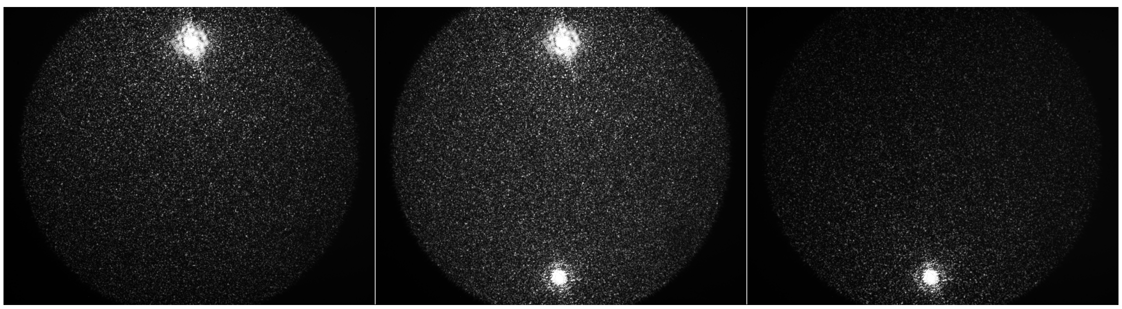

Figure 4.12: Speckle images of 10μm monodisperse SiO_2 beads acquired using scatterometer setup. Left: Top illuminator activated; Center: Both illuminators activated; Right: Bottom illuminator activated

4.12 Note: Proposal:Expected Results

We have identified imaging configurations that produce high-contrast speckle images with well-resolved speckle grains through HDR acquisition and proper camera specifications. Examples of images we have acquired to date are shown in Figure 4.12. These speckle images are high-contrast which is indicative of a suitable beamwidth (5mm) for the sample's scattering cross-section, and the speckle grains are well-resolved, meaning the camera's angular resolution is sufficient.

A preliminary result that indicates we are on the right track is computing and plotting 2D speckle correlation and showing that this correlation increases with decreasing sample optical density as suggested by Equation **??**. Next, we plan to acquire phase functions of materials similar those acquired in [1] over a larger range of scattering angles. Figure 4.13 shows our planned extension of the scattering angle range. If our phase functions agree with [1], it will help validate our acquisition configuration and correlation scripts.

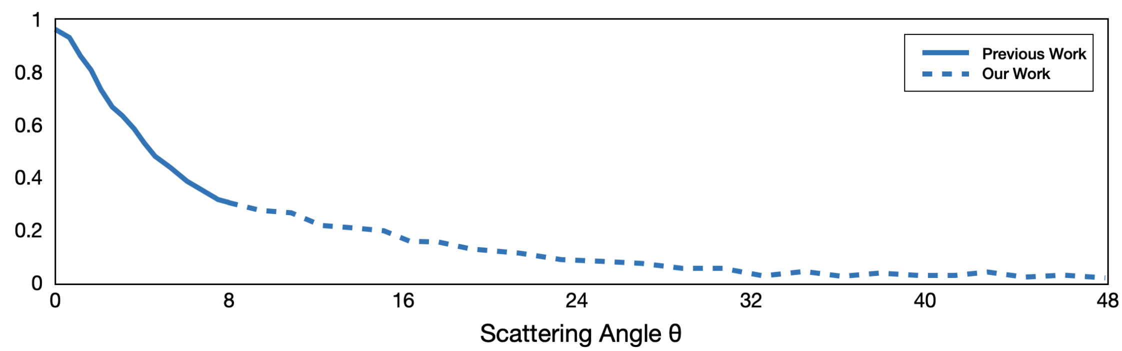

Figure 4.13: An expected result is acquiring the scattering phase function for a larger range of scattering angles than the literature.

Chapter 5

Acquisition

In this chapter, we delve into the scatterometer design as well as the calibration and alignment process.

5.1 Scattering Samples

5.2 Acquisition

5.3 Maximizing Light Scattered Towards Camera

5.4 Illumination Polarization

The Verdi output beam is linearly polarized and passed through single-mode (SM) fibers prior to illuminating scattering samples with the resulting beam having an unknown polarization state due to use of non-polarization-maintaining fibers. This raises several questions 1) What is the beam's polarization state?; 2) Is it constant?; and 3) What is the optimal polarization state of the output beam to maximize light transmission into the sample?

Literature suggests the output beam will have an elliptical polarization state (1) that is variable/unstable (2) due to variable birefringence induced in SM fibers caused by variable internal stresses and temperature fluctuations.

The output polarization state's stability was characterized by placing a power meter photodiode with a static LPF to measure the power of a collimator on the dual collimator stand attached to the RT-5 rail. The measured power for 10 sweeps of the RT-5 through a range of 280 degrees is shown in Figure 5.1. There is a clear relationship between the measured power through an LPF and the RT-5 stage position which suggests the polarization state does not remain constant across illumination angles. The ellipticity

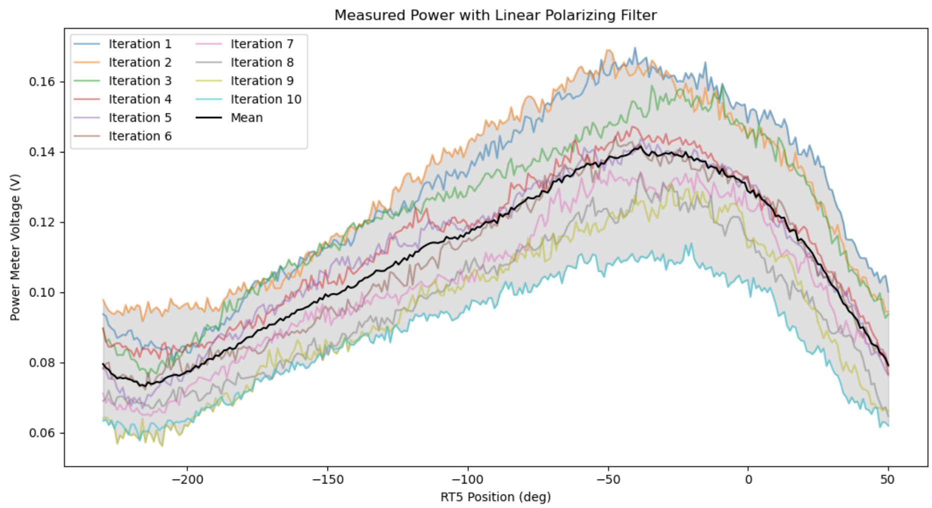

Figure 5.1

was not investigated due to requiring a circular polarizing filter (CPF). Fluctuations in measured power across sweeps was due to insertion losses caused by motion of unstable FC/PC fiber connectors on the RT-5 rail. Fixing those connectors to the rail saw significant reductions in fluctuations.

Polarization state for Figure 5.1:

- $S_0 = 0.200696$
- $S_1 = -0.028441$
- $S_2 = 0.06834$
- $S_DoP = \sqrt{S_1^2 + S_2^2}/S_0 \approx 0.37$

5.4.1 Optimizing Illumination & Sample Orientation to Maximize Light Transmission

Given a linearly polarized illumination laser beam, an acquisition sensor offset by some scattering angle, and a scattering sample inside a glass cell, the goal is to determine 1) the optimal sample orientation and 2) the optimal angle of polarization to maximize light transmitted from the illuminator to the acquisition sensor.

Fresnel Formulae

The contents in this section are paraphrased from [7]. Consider a plane wave with amplitude A incident on a surface. The electric and magnetic field vectors can be decomposed into two components parallel and perpendicular to the surface plane. The incident electric field is

$$E^{(i)} = \begin{bmatrix} -A_{||} \cos\theta_i e^{-i\tau_i} \\ A_{\perp} e^{-i\tau_i} \\ A_{||} \sin\theta_i e^{-i\tau_i} \end{bmatrix} \tag{5.1}$$

where E_x, E_z are in the plane, and E_y is along the plane normal. The complex exponential argument is defined

$$\tau_i = \omega\left(t - \frac{\mathbf{r}^\intercal \mathbf{s}^{(i)}}{v}\right) = \omega\left(t - \frac{x \sin\theta_i + z \cos\theta_i}{v}\right) \tag{5.2}$$

The magnetic field vector H is written similarly through the relation $H = \sqrt{\epsilon}\mathbf{s} \times \mathbf{E}$. where $\mathbf{s}$ is the light's velocity vector. If T and R denote the transmitted and reflected amplitudes, then the transmitted field is

$$E^{(t)} = \begin{bmatrix} -T_{||} \cos\theta_t e^{-i\tau_t} \\ T_{\perp} e^{-i\tau_t} \\ T_{||} \sin\theta_t e^{-i\tau_t} \end{bmatrix}, \tag{5.3}$$

and the reflected field is

$$E^{(r)} = \begin{bmatrix} -R_{||} \cos\theta_r e^{-i\tau_r} \\ R_{\perp} e^{-i\tau_r} \\ R_{||} \sin\theta_r e^{-i\tau_r} \end{bmatrix}. \tag{5.4}$$

The tangential components of the electric and magnetic fields must be continuous across the boundary, resulting in four boundary conditions:

$$E_x^{(i)} + E_x^{(r)} = E_x^{(t)} \quad E_y^{(i)} + E_y^{(r)} = E_y^{(t)} \tag{5.5}$$

$$H_x^{(i)} + H_x^{(r)} = H_x^{(t)} \quad H_y^{(i)} + H_y^{(r)} = H_y^{(t)} \tag{5.6}$$

These boundary conditions can be solved for an expression of the transmitted and reflected amplitudes components by using the Maxwell relation $n = \sqrt{\epsilon}$

$$T_{||} = \frac{2n_1 \cos\theta_i}{n_2 \cos\theta_i + n_1 \cos\theta_t} A_{||} \quad T_{\perp} = \frac{2n_1 \cos\theta_i}{n_1 \cos\theta_i + n_2 \cos\theta_t} A_{\perp} \tag{5.7}$$

$$R_{||} = \frac{n_2 \cos\theta_i - n_1 \cos\theta_t}{n_2 \cos\theta_i + n_1 \cos\theta_t} A_{||} \quad R_{\perp} = \frac{n_1 \cos\theta_i - n_2 \cos\theta_t}{n_1 \cos\theta_i + n_2 \cos\theta_t} A_{\perp} \tag{5.8}$$

Effects of Polarization on Fresnel Formulae

The light intensity is

$$S = \frac{c}{4\pi}\sqrt{\epsilon}E^2 = \frac{cn}{4\pi}E^2 \tag{5.9}$$

The resulting energy incident on a surface with unit area A is

$$J^{(i)} = S^{(i)} \cos\theta_i = \frac{cn_1}{4\pi}|A|^2 \cos\theta_i \tag{5.10}$$

with reflected and transmitted energies

$$J^{(r)} = \frac{cn_1}{4\pi}|R|^2 \cos\theta_i \quad and \quad J^{(t)} = \frac{cn_2}{4\pi}|T|^2 \cos\theta_t. \tag{5.11}$$

The reflectivity and transmissivity are

$$\mathcal{R} = \frac{J^{(r)}}{J^{(i)}} = \frac{|R|^2}{|A|^2} \quad and \quad \mathcal{T} = \frac{J^{(t)}}{J^{(i)}} = \frac{|T|^2}{|A|^2} \tag{5.12}$$

which satisfy the law of conservation of energy by summing to 1

$$\mathcal{R} + \mathcal{T} = 1. \tag{5.13}$$

The reflectivity and transmissivity are functions of polarization with respect to the parallel and perpendicular directions. If the incident electric field **E** makes an angle α_i with respect to the plane, the parallel and perpendicular area components are

$$A_{||} = A\cos\alpha_i \quad and \quad A_{\perp} = A\sin\alpha_i \tag{5.14}$$

The parallel energy component of the incident light is

$$\begin{aligned} J_{||}^{(i)} &= \frac{cn_1}{4\pi}|A_{||}|^2 \cos\theta_i \\ &= \frac{cn_1}{4\pi}|A|^2 \cos^2\alpha_i \cos\theta_i \\ &= J^{(i)} \cos^2\alpha_i \end{aligned} \tag{5.15}$$

with that of the perpendicular component following similarly:

$$J_{\perp}^{(i)} = J^{(i)} \sin^2\alpha_i. \tag{5.16}$$

The reflectivity in terms of polarized light is

$$\begin{aligned} \mathcal{R} = \frac{J^{(r)}}{J^{(i)}} &= \frac{J_{||}^{(r)} + J_{\perp}^{(r)}}{J^{(i)}} \\ &= \frac{J_{||}^{(r)}}{J_{||}^{(i)}} \cos^2\alpha_i + \frac{J_{\perp}^{(r)}}{J_{\perp}^{(i)}} \sin^2\alpha_i \\ &= \mathcal{R}_{||} \cos^2\alpha_i + \mathcal{R}_{\perp} \sin^2\alpha_i, \end{aligned} \tag{5.17}$$

and the transmissivity is

$$\mathcal{T} = \mathcal{T}_{||} \cos^2\alpha_i + \mathcal{T}_{\perp} \sin^2\alpha_i. \tag{5.18}$$

Reflectivity and transmissivity must satisfy conservation of energy respectively:

$$\mathcal{R}_{||} + \mathcal{T}_{||} = 1, \qquad \mathcal{R}_{\perp} + \mathcal{T}_{\perp} = 1. \tag{5.19}$$

When light is incident normal to the surface, $\alpha_i = 0$ for all E-field orientations, meaning there is no distinction between the parallel and perpendicular components, and the reflectivity and transmissivity are written

$$\mathcal{R} = \left(\frac{n-1}{n+1}\right)^2, \qquad \mathcal{T} = \frac{4n}{(n+1)^2} \tag{5.20}$$

where $n = n_2/n_1$.

Fresnel Relations as Mueller Matrices

Transmission

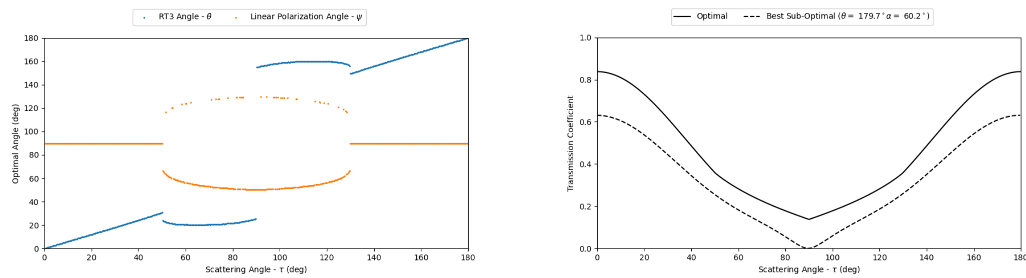

Figure 5.2

Scattering This section summarizes the results in [6]. Assuming light with wavevector k is scattered from a small sphere with radius a with scattering amplitude coefficient $a_1 \in \mathbb{C}$, the scattered field at distance r from the scatterer, the Mueller matrix is

$$\mathbf{M}_s = \frac{9|a_1|^2}{4k^2r^2}\begin{bmatrix} \frac{1}{2}(1+\cos^2\theta) & \frac{1}{2}(\cos^2\theta - 1) & 0 & 0 \\ \frac{1}{2}(\cos^2\theta - 1) & \frac{1}{2}(1+\cos^2\theta) & 0 & 0 \\ 0 & 0 & \cos\theta & 0 \\ 0 & 0 & 0 & \cos\theta \end{bmatrix} \tag{5.21}$$

where the scattering coefficient is defined

$$a_1 = -\frac{i2x^3}{e}\frac{m^2-1}{m^2+2} - \frac{i2x^5}{5}\frac{(m^2-2)(m^2-1)}{(m^2+2)^2} \tag{5.22}$$

with scale factor and relative refractive index

$$x = ka = \frac{2\pi N a}{\lambda}, \qquad m = \frac{N_1}{N} = \frac{k_1}{k} \tag{5.23}$$

where N and N_1 are the medium's and particle's refractive indices respectively. The scattering Mueller matrix is defined within the scattering plane containing the incoming and outgoing directions as well as the scattering particle.

Simulation Results

Unpolarized Beam

Linearly Polarized Beam

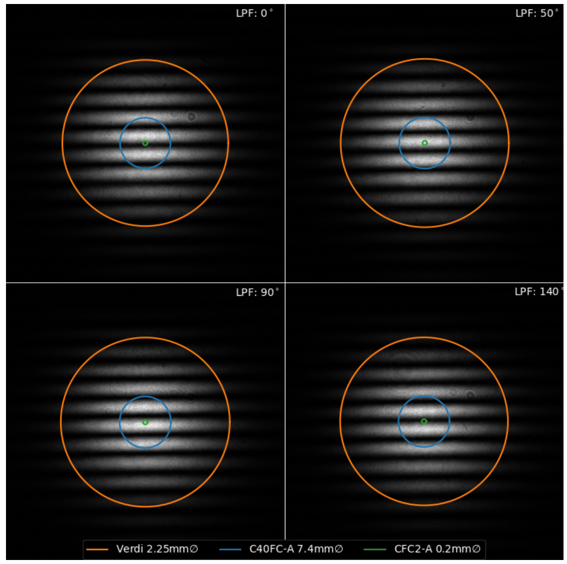

Figure 5.3

5.4.2 Simulation

5.4.3 Depolarizer Spatial Characterization

One option is to depolarize the illumination beams via Thorlabs DPP25-A liquid crystal polymer depolarizer. This optic is a series of linear polarizing strips each oriented in 45-degree increments. The incident beam is passed through these strips, and the output beam is a combination of linear polarization states with different angles of polarization. Since strips are distributed spatially, the output beam's polarization state is a function of the incident beam size.

The affect of beam size on output polarization state was characterized by measuring the spatial distribution of polarization state using a camera. The Verdi output beam was coupled into a 2-meter single-mode fiber whose output was collimated using Thorlabs C40FC-A. That beam was passed through the depolarizer mounted on Thorlabs CRM1PT followed by a linear polarizing filter mounted on Thorlabs CRM1T. The beam was then passed through an ND=2.0 filter prior to measurement by the camera. The camera was Grasshopper3 GS3-PGE-91S6M with a Leica Summicron-A 50mm 1:2 lens focused at its shortest working distance (1:6.6 magnification). Acquisition consisted of rotating the LPF in 10-degree increments over a range of 170 degrees and acquiring a 16-bit image for each LPF orientation.

The intensity profiles of the depolarized beam for four LPF orientations is shown in Figure 5.3. Each profile is a Gaussian-enveloped sinusoid whose phase changes with the LPF orientation. Each image is overlaid with $1/e^2$ beam diameters for two collimators' output beams and the Verdi output beam. The

C40FC-A and Verdi beam profiles are large enough to cover at least a full period of the depolarizer's structure, while the CFC2-A beam does not. Therefore, the depolarizer would not be effective if used with the CFC2-A collimator.

Chapter 6

Appendices

6.1 Calibration Target Design

A contiguous calibration target was chosen initially for beam direction estimation. However, the variable albedo due to ink created structured noise. This caused estimates of beams partially overlapping black regions to become biased towards the white regions. As a result, a window was added to the target allowing all centroiding estimates to occur on a surface of constant albedo. See Figure 6.1.

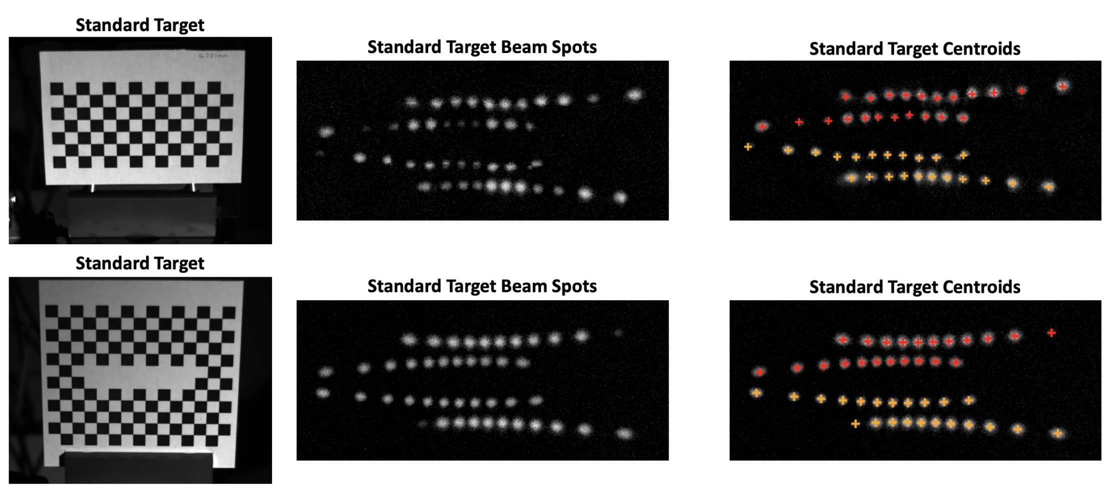

Figure 6.1: Top row: Original target used for calibration caused irregular beam spot shapes which produced noisy centroids. Bottom row: Windowed target used now to avoid albedo issues when imaging beam spots.

6.2 Sample Preparation

Equipment Required

- Microscope slides (two per sample)
- Dropper or syringe with capacity greater than or equal to the target sample volume
- Ethanol
- Isopropyl alcohol
- Non-abrasive working surface to prevent scratching slides

Part No.	Vendor	Qty.	Description
30392080	Ohaus	1	Dry Block Tube Heater
30400154	Ohaus	1	Module Block 20mm 8 Wells
30400193	Ohaus	1	Module Block 50, 15, 1.5mL
FA10006M	Gilson	1	P1000L 100-1000uL pipette
AB0576	Thermo Fisher	1	25uL gene frame
AB0577	Thermo Fisher	1	65uL gene frame
AB0578	Thermo Fisher	1	125uL gene frame
GEMINI-20-BLK	American Weigh Scales	1	Milligram scale + boat
F167014	Gilson	1	D1000 tip reload pack
4916345	Scientific Labwares	1	oval lab spoon
CHWB 1020B	Eisco	1	Water squeeze bottle
CHWB 1030	Eisco	1	IPA squeeze bottle
CHWB 1037	Eisco	1	Ethanol squeeze bottle
A20090-50.0	RPI	1	Agarose, 50 G
???	Swift	1	Microscope
EC 1.3MP	Swift	1	Microscope camera
W5-4	Fisher Chemical	1	4L HPLC Water
904341-2G	Millipore Sigma	1	Silica monodisperse 3um spheres
34155	Kimtech	1	Kimwipes
MPR-50504	Med Pride	1	Nitrile gloves
55105	SPL Life Sciences	1	5mL centrifuge snap tubes
50215	SPL Life Sciences	1	15mL centrifuge snap tubes
???		1	Microfiber towel

1. Clean all labware with IPA and dry with Kimtech wipes. Clean slides with IPA and dry with optical cleaning cloth.

2. Pour 5 mL HPLC water in a 15 mL tube using a squeeze bottle.

3. Set the tube heater to 95°C and place the 15 mL tube in a heating block.

4. Once the heater has reach the set point, place a clean 5 mL tube in a heating block. Let both tubes remain in the block for 5 minutes.

5. Cut _ mm off the end of a clean pipette tip so its opening is 2 mm in diameter.
6. Transfer heated HPLC water from the 15 mL tube to the 5 mL tube.
7. Measure _ mg agarose powder in a clean weighting boat and add it to the 5 mL tube. Place it in a heating block for 10 minutes, using bottoms-up agitation every 2 minutes.
8. While waiting, measure _ mg silica beads in the weigh boat and set aside.
9. Attach a gene frame to a microscope slide.
10. Once the water has been heated for 10 minutes, place the slide on a heating block. Then add the silica beads to the agarose solution and let the suspension heat for 5 minutes, using bottoms-up agitation every minute.
11. Using a 1 mL pipette, cycle the liquid within the 5 mL tube several times.
12. Ensure the pipette's volume is set to 96% of the gene frame's volume.

    Note: The following sequence should occur quickly. Otherwise the suspension will cool and begin gelling, reducing the sample quality:
13. Using heat-resistant gloves, remove the heated slide and place it on a microfiber towel.
14. Intake the desired volume of the suspension and aliquot it while moving the pipette tip across the area of the gene frame. This will minimize the height of the liquid and will prevent overflow when placing the slide cover on the gene frame.
15. Using another microscope slides, attach the slide cover from one side to another, lengthwise along the gene frame.
16. Press the slide flat against the slide cover and leave it in place to ensure the cover is parallel with the surface of the sample slide.
17. Weigh-out the amount using a scooper and clean weigh boat
18. Combine microspheres with _ mL ethanol in a centrifuge tube
    - Micro sphere volume: $14.137\mu m^3 = 1.4137 \times 10^{-11} cm^3$
    - Micro spheres per gram: $3.1 \times 10^{11} \frac{sphere}{g} = \frac{1\ cm^3}{2.196\ g} \left(\frac{10^4\ \mu m}{1\ cm}\right)^3 \frac{1}{(\frac{4}{3}\pi 1.5^3)\ \mu m^3}$
    - Ethanol Volume: $\frac{3.1\times10^{11}\ spheres}{1\ g} \cdot \frac{1.4137\times10^{-11} cm^3}{1\ sphere} \cdot \frac{1\ mL}{1\ cm^3} \cdot 125 \cdot x\ grams$

19. Measure-out 0.1 g of agarose powder and place in second tube
20. Fill second tube with 10 mL HPCL water
21. Fill 10 tubes with HPCL water
22. Insert all 12 tubes in heating block
23. Set the mixer to _ degrees Celsius and begin heating the tubes.
24. After _ minutes, start mixing the tubes at _ RPM for _ minutes.
25. Once done, pour the water tubes into a TBD container and place the slides in the water.
26. Pour the microsphere-Ethanol mixture into the agarose mixture and resume mixing and heating for _ minutes (depending on time required to heat-up slides).
27. Remove slides, dry them, attach gene frames, and place on non-abrasive surface. The next few steps should be completed quickly to avoid the slides cooling too much.
28. When mixing is complete, remove tube and agitate 20 times using the bottoms-up method
29. Place the mixture back in the mixer and use a pipette to transfer liquid to the center of the gene frame. The amount transferred should match the volume of the gene frame.
30. Sandwich the sample using the top face of another microscope slide (not the side that was facing down on the table). While sandwiching, touch the slides as far away from the gene frame as possible, and on the edges.
31. Place on the rotator at _ RPM for _ minutes (need to calculate cooling rate). The liquid and slides should now be at a uniform temperature.
32. Inspect the sample using a microscope objective to determine the uniformity. Need to develop procedure for this. Maybe 8 locations (3 along top, 3 along bottom, two intermediate positions along sample center line). Then compute variance of number of particles visible across images? Use that as a benchmark.
33. Clean pipette internals, glassware using IPA

6.3 Ziegler-Nichols Tuning Method

The Ziegler-Nichols tuning method is a PID tuning heuristic based on two principal characteristics affecting process controllability [39]:

1. The ultimate gain K_u is the proportional gain above which oscillations will increase to a maximum amplitude, and below which oscillations will decay to zero response.
2. The period of oscillation T_u is the period in minutes of constant-amplitude oscillations corresponding to a P controller with gain K_u.

It defines the necessary proportional (K_p), integral (K_i), and derivative (K_d) gains for control stability given the ultimate gain and period of oscillation.

Table 6.1: Ziegler-Nichols method

Control Type	K_p	T_i	T_d	K_i	K_d
P	0.5 K_u	-	-	-	-
PI	0.45 K_u	0.83 T_u	-	0.54 K_u/T_u	-
PD	0.3 K_u	-	0.125 T_u	-	0.10 K_uT_u
classic PID	0.6 K_u	0.5 T_u	0.125 T_u	1.2 K_u/T_u	0.075 K_uT_u
Pessen Integral Rule	0.7 K_u	0.4 T_u	0.15 T_u	1.75 K_u/T_u	0.105 K_uT_u
some overshoot	0.33 K_u	0.50 T_u	0.33 T_u	0.66 K_u/T_u	0.11 K_uT_u
no overshoot	0.20 K_u	0.50 T_u	0.33 T_u	0.40 K_u/T_u	0.066 K_uT_u

Note: Alternative is Tyreus-Luyben method [23] For example, assume the error is directly proportional to the actuation distance of a translation stage. If the initial

Bibliography

[1] Marina Alterman, Evgeniia Saiko, and Anat Levin. Direct acquisition of volumetric scattering phase function using speckle correlations. In *SIGGRAPH Asia 2022 Conference Papers*, pages 1–9, 2022.

[2] Guillaume Bal. Inverse transport theory and applications. *Inverse Problems*, 25(5):053001, 2009.

[3] Chen Bar, Marina Alterman, Ioannis Gkioulekas, and Anat Levin. A monte carlo framework for rendering speckle statistics in scattering media. *ACM Transactions on Graphics (TOG)*, 38(4):1–22, 2019.

[4] Bruce J Berne and Robert Pecora. *Dynamic light scattering: with applications to chemistry, biology, and physics*. Courier Corporation, 2000.

[5] David A Boas, Dana H Brooks, Eric L Miller, Charles A DiMarzio, Misha Kilmer, Richard J Gaudette, and Quan Zhang. Imaging the body with diffuse optical tomography. *IEEE signal processing magazine*, 18(6):57–75, 2001.

[6] Craig F Bohren and Donald R Huffman. *Absorption and scattering of light by small particles*. John Wiley & Sons, 2008.

[7] Max Born and Emil Wolf. *Principles of optics: electromagnetic theory of propagation, interference and diffraction of light*. Elsevier, 2013.

[8] Chengqian Che, Fujun Luan, Shuang Zhao, Kavita Bala, and Ioannis Gkioulekas. Towards learning-based inverse subsurface scattering. In *2020 IEEE International Conference on Computational Photography (ICCP)*, pages 1–12. IEEE, 2020.

[9] William M Cornette and Joseph G Shanks. Physically reasonable analytic expression for the single-scattering phase function. *Applied optics*, 31(16):3152–3160, 1992.

[10] Turgut Durduran, Regine Choe, Wesley B Baker, and Arjun G Yodh. Diffuse optics for tissue monitoring and tomography. *Reports on progress in physics*, 73(7):076701, 2010.

[11] Philip Dutre, Philippe Bekaert, and Kavita Bala. *Advanced global illumination.* AK Peters/CRC Press, 2018.

[12] Thomas J Farrell, Michael S Patterson, and Brian Wilson. A diffusion theory model of spatially resolved, steady-state diffuse reflectance for the noninvasive determination of tissue optical properties in vivo. *Medical physics*, 19(4):879–888, 1992.

[13] Ronald Aylmer Fisher. Dispersion on a sphere. *Proceedings of the Royal Society of London. Series A. Mathematical and Physical Sciences*, 217(1130):295–305, 1953.

[14] Jeppe Revall Frisvad, Niels Jørgen Christensen, and Henrik Wann Jensen. Computing the scattering properties of participating media using lorenz-mie theory. In *ACM SIGGRAPH 2007 papers*, pages 60–es. 2007.

[15] Ioannis Gkioulekas, Anat Levin, and Todd Zickler. An evaluation of computational imaging techniques for heterogeneous inverse scattering. In *Computer Vision–ECCV 2016: 14th European Conference, Amsterdam, The Netherlands, October 11-14, 2016, Proceedings, Part III 14*, pages 685–701. Springer, 2016.

[16] Ioannis Gkioulekas, Bei Xiao, Shuang Zhao, Edward H Adelson, Todd Zickler, and Kavita Bala. Understanding the role of phase function in translucent appearance. *ACM Transactions on graphics (TOG)*, 32(5):1–19, 2013.

[17] Ioannis Gkioulekas, Shuang Zhao, Kavita Bala, Todd Zickler, and Anat Levin. Inverse volume rendering with material dictionaries. *ACM Transactions on Graphics (TOG)*, 32(6):1–13, 2013.

[18] Kenji Hara, Ko Nishino, and Katsushi Ikeuchi. Mixture of spherical distributions for single-view relighting. *IEEE Transactions on Pattern Analysis and Machine Intelligence*, 30(1):25–35, 2007.

[19] Louis George Henyey and Jesse L Greenstein. Diffuse radiation in the galaxy. *Annales d'Astrophysique, Vol. 3, p. 117*, 3:117, 1940.

[20] Hendrik Christoffel Hulst and Hendrik C van de Hulst. *Light scattering by small particles.* Courier Corporation, 1981.

[21] Pramook Khungurn, Daniel Schroeder, Shuang Zhao, Kavita Bala, and Steve Marschner. Matching real fabrics with micro-appearance models. *ACM Trans. Graph.*, 35(1):1–1, 2015.

[22] Matthew M Loper and Michael J Black. Opendr: An approximate differentiable renderer. In *Computer Vision–ECCV 2014: 13th European Conference, Zurich, Switzerland, September 6-12, 2014, Proceedings, Part VII 13*, pages 154–169. Springer, 2014.

[23] William L Luyben. Simple method for tuning siso controllers in multivariable systems. *Industrial & Engineering Chemistry Process Design and Development*, 25(3):654–660, 1986.

[24] Adolfo Munoz, Jose I Echevarria, Francisco J Seron, Jorge Lopez-Moreno, Mashhuda Glencross, and Diego Gutierrez. Bssrdf estimation from single images. In *Computer Graphics Forum*, volume 30, pages 455–464. Wiley Online Library, 2011.

[25] Srinivasa G Narasimhan, Mohit Gupta, Craig Donner, Ravi Ramamoorthi, Shree K Nayar, and Henrik Wann Jensen. Acquiring scattering properties of participating media by dilution. In *ACM SIGGRAPH 2006 Papers*, pages 1003–1012. 2006.

[26] Merlin Nimier-David, Sébastien Speierer, Benoît Ruiz, and Wenzel Jakob. Radiative backpropagation: An adjoint method for lightning-fast differentiable rendering. *ACM Transactions on Graphics (TOG)*, 39(4):146–1, 2020.

[27] Merlin Nimier-David, Delio Vicini, Tizian Zeltner, and Wenzel Jakob. Mitsuba 2: A retargetable forward and inverse renderer. *ACM Transactions on Graphics (ToG)*, 38(6):1–17, 2019.

[28] Jan Novák, Iliyan Georgiev, Johannes Hanika, and Wojciech Jarosz. Monte carlo methods for volumetric light transport simulation. In *Computer graphics forum*, volume 37, pages 551–576. Wiley Online Library, 2018.

[29] Marios Papas, Christian Regg, Wojciech Jarosz, Bernd Bickel, Philip Jackson, Wojciech Matusik, Steve Marschner, and Markus Gross. Fabricating translucent materials using continuous pigment mixtures. *ACM Transactions on Graphics (TOG)*, 32(4):1–12, 2013.

[30] Dave J Pine, Dave A Weitz, JX Zhu, and Eric Herbolzheimer. Diffusing-wave spectroscopy: dynamic light scattering in the multiple scattering limit. *Journal de Physique*, 51(18):2101–2127, 1990.

[31] Lord Rayleigh. Xxxiv. on the transmission of light through an atmosphere containing small particles in suspension, and on the origin of the blue of the sky. *The London, Edinburgh, and Dublin Philosophical Magazine and Journal of Science*, 47(287):375–384, 1899.

[32] LO Reynolds and NJ McCormick. Approximate two-parameter phase function for light scattering. *JOSA*, 70(10):1206–1212, 1980.

[33] Denis Sumin, Tobias Rittig, Vahid Babaei, Thomas Nindel, Alexander Wilkie, Piotr Didyk, Bernd Bickel, J KŖivánek, Karol Myszkowski, and Tim Weyrich. Geometry-aware scattering compensation for 3d printing. *ACM Transactions on Graphics*, 38(4), 2019.

[34] Bertrand Thierry, Xavier Antoine, Chokri Chniti, and Hasan Alzubaidi. μ-diff: An open-source matlab toolbox for computing multiple scattering problems by disks. *Computer Physics Communications*, 192:348–362, 2015.

[35] Jiajun Wu, Joshua B Tenenbaum, and Pushmeet Kohli. Neural scene de-rendering. In *Proceedings of the IEEE Conference on Computer Vision and Pattern Recognition*, pages 699–707, 2017.

[36] Douglas R Wyman, Michael S Patterson, and Brian C Wilson. Similarity relations for the interaction parameters in radiation transport. *Applied optics*, 28(24):5243–5249, 1989.

[37] Shuang Zhao, Ravi Ramamoorthi, and Kavita Bala. High-order similarity relations in radiative transfer. *ACM Transactions on Graphics (TOG)*, 33(4):1–12, 2014.

[38] Quan Zheng, Gurprit Singh, and Hans-Peter Seidel. Neural relightable participating media rendering. *Advances in Neural Information Processing Systems*, 34:15203–15215, 2021.

[39] John G Ziegler and Nathaniel B Nichols. Optimum settings for automatic controllers. *Transactions of the American society of mechanical engineers*, 64(8):759–765, 1942.